UNIVERSITÀ DEGLI STUDI DI PADOVA

Dipartimento di Fisica e Astronomia “Galileo Galilei”

CORSO DI LAUREA MAGISTRALE IN FISICA

TESI DI LAUREA

# Quantum dots as sources of quantum light

Relatore :
**Prof. Giovanni Mattei**

Laureando :
**Filippo Zorzi**

**Anno Accademico 2018 / 2019**

# Contents

**Introduction** **iii**

**1 Theory** **1**
- 1.1 Quantum Dots . . . . . 1
  - 1.1.1 Self-assembled Quantum Dots . . . . . 2
  - 1.1.2 Site-controlled Quantum Dots . . . . . 3
- 1.2 Quantum Dots energy structure . . . . . 3
- 1.3 Excitation of a QD . . . . . 8
  - 1.3.1 Above band excitations . . . . . 9
  - 1.3.2 Resonant excitations . . . . . 12
- 1.4 Photon statistics . . . . . 14
- 1.5 Photons indistinguishability . . . . . 18

**2 Development of the experimental Setup** **23**
- 2.1 Cooling system . . . . . 23
- 2.2 Imaging of the sample . . . . . 25
- 2.3 Spectroscopy methods . . . . . 25
  - 2.3.1 Princeton Instruments spectrometer . . . . . 25
  - 2.3.2 Self-made spectrometer . . . . . 28
- 2.4 Optical line characterization . . . . . 30
- 2.5 Pulse stretcher . . . . . 33
- 2.6 Interferometer . . . . . 39

**3 Experimental results** **45**
- 3.1 A single Quantum Dot spectrum . . . . . 45
- 3.2 Measurements of $g^{(2)}(\tau)$ . . . . . 48
  - 3.2.1 Exciton autocorrelation . . . . . 48

**4 Conclusions** **51**

**A Fock and coherent states** **55**

**Bibliography** **58**

# Introduction

Semiconductor Quantum dots are attracting an increasing interest from scientific community, due to their peculiar optical properties. They possess many different applications in various research and industrial fields. With quantum dots it is possible to produce for example solar cells, or new generation screens. An important property is their discrete energy spectrum, and then their capability of emitting single photons, or entangled photon pairs, under an appropriate optical excitation. This property is especially useful when applied to quantum photonics and to quantum information protocols. In fact the possibility of using photons as qubits to encode, transmit and process quantum information has been considered and investigated many times, due to their low decoherence, high-speed transmission and the possibility of using classical photonic technologies [1] [2].

The goal of this thesis is the characterization of a single semiconductor quantum dots as single photon source, for its use in quantum information protocols.

This goal will be achieved through the design, building and the optimization of some optical devices, such as a spectroscopy set-up, a pulse stretcher and an interferometer. The thesis is divided into three different chapters:

- **Chapter 1 :** In the first chapter the main physics regarding quantum dots will be explained. It will start from their fabrication, briefly explaining the differences between the *Self-assembled quantum dots* and the *Site controlled quantum dots*. Then their energy structure will be explained, with a focus on the first two excited states, the exciton (X) and the bi-exciton (XX). These two states are the most significant states of a quantum dot for generation of quantum light and entangled photon pairs. After this part the optical excitation schemes of a quantum dot will be explained, dividing them into *above band* and *in band* excitations. Then there is a section regarding the statistics of the emitted photons, and the methods useful to investigate the quantum nature of light emission. The last part is about the photon indistinguishability, and consequently the importance of the coherence length in quantum photonics.
- **Chapter 2 :** The second chapter will explain all the experimental setup and the reasons which led us to build it with that configuration. It will start with the description of the cooling system, which cooled down the sample to 4 K. Then the imaging system will be explained, that allowed us to see the sample and align and focus the excitation laser on it. For investigation of the Quantum dot emission,

two different spectroscopic systems were used : a commercial *Princeton instruments* spectrometer, useful to get a quick overview of the spectra of the excited quantum dot, and a self-made spectrometer, used to measure important parameters for the characterization of the photon emission, such as the *second order correlation function*. Afterwards the design and building of a pulse stretcher will be presented. A pulse stretcher allows us to easily tune the time duration of a pulse from a pulsed laser source (in our case, a Ti:Sapphire pulsed laser with 140 fs pulse duration). The set-up of a pulse stretcher is essential in order to obtain resonant excitation of a quantum dot. At last, the principles ruling interference in a Michaelson interferometer (which was built as part of the experimental setup) will be presented, and its importance for the measurement of coherence length of the emitted photons.

- **Chapter 3 :** In the third chapter the experimental results will be shown. These include some spectra, taken under above band excitation, and using a continuous wave He-Ne laser. Using these spectra, and measuring the counts corresponding to different emission lines and their dependence under increasing excitation powers, it is possible to discriminate between the emission lines corresponding to different excitation processes (in our case the exciton and the biexciton). Once these lines have been identified, it was possible to separate the paths followed by the emitted photons with the self-made spectrometer, and measure the second order correlation function of the exciton photons. In this way the quantum nature of the light emitted by a single semiconductor quantum dot has been proved.

# Chapter 1

# Theory

## 1.1 Quantum Dots

The foundation of quantum photonic experiments is based on the generation, manipulation and detection of quantum light. In the case of single photons, they are ideally created by two-level systems. There are many two-level systems that can be used, such as single atoms, molecules or color centers [3]. In addition to these systems, there are other options. A particular atom-like system that can be described as a two level system is a semiconductor quantum dot (QD). Quantum dots can be created embedding a semiconductor with a small bandgap in between another semiconductor with a larger bandgap.
Quantum dots are attracting an increasing interest from the scientific community, because of their unique and interesting properties, making them useful for multiple applications in both research and industry. For example, QDs can be used as light-emitting diodes or solar cells [4] [5] [6].
QDs are used in Quantum photonics due to their ability to generate non-classical light. Talking about non-classical light refers to those states that cannot be emitted by a classical source, like a thermal light or a laser. If excited under resonant excitation, these devices become in fact a quasi deterministic single-photon sources with high emission efficiency. Several interesting properties have been already demonstrated for light emitted from quantum dots, such as two-photon interference [7] and polarization entanglement [8]. These properties make QDs very attractive for several applications in the fields of quantum cryptography, quantum communication and quantum information [ref]. Furthermore, Quantum Dots can easily be integrated in solid-state systems, and they are easy to use in integrated photonics circuits. It is possible to tune their emission spectrum in a wide range - from 850 to 1400 nm - by changing their size. The emission spectrum can be changed modifying the QD geometry [9] or its composition.

In order to exploit quantum dots' peculiar properties, it is crucial to have a strong three dimensional spatial confinement of the semiconductor material. This means that quantum dots cannot be bigger than $\sim 10$ nm. If they are bigger than 10 nm, they start losing their quantum confinement properties, and start behaving as a bulk material. There are several ways to produce quantum dots, which will be described in the subsequent sections.

### 1.1.1 Self-assembled Quantum Dots

The lattice parameters mismatch between two different semiconductors gives rise to strain when the two materials are deposited on top of each other. This circumstance is exploited in the *Stranski-Krastanov* growth method [10][11]. In this method a material with small band gap is deposited onto a substrate with larger bandgap. Here initially the layer formed has the same lattice parameter as the substrate, with a strong deformation in the chemical bonds. As the thickness increases, the total energy of the system does also, until it reaches a critical value. Once reached this point, different energy relaxation processes appear, producing dislocations, or increasing the surface through the formation of tridimensional nucleus (dots) (Figure 1.1). Not all the atoms form these nucleus, a small layer of them remains on all the surface, which is called the *wetting layer.* This layer can influence the physics of the dot [12].
The size of these islands can be controlled by the amount of material deposited. In order to complete the three dimensional quantum confinement, another layer of the semiconductor with larger band gap is deposited [1].

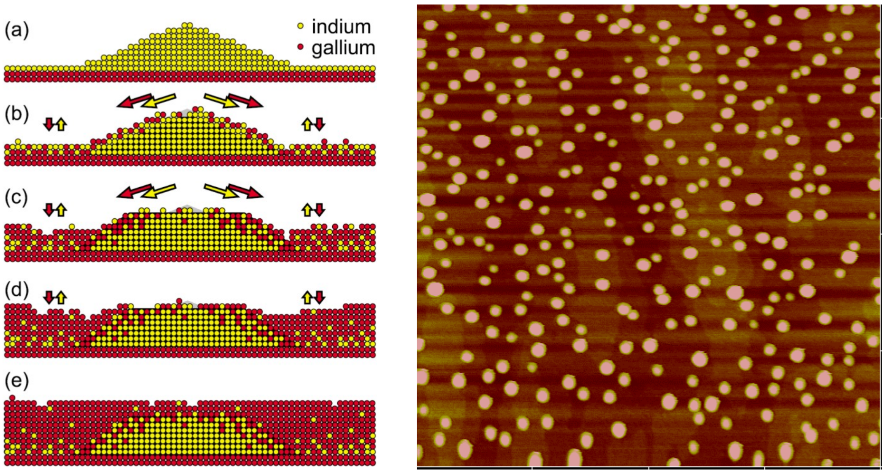

Figure 1.1: Left: illustration of the capping process of a InAs Quantum dots grown onto GaAs layers. Image from [13]. Right : Atomic Force Microscope image of uncapped self-assembled InAs quantum dots. The image covers one square micron. Image from [14].

As the formation of these islands is a stochastic process, the position of the quantum dot can not be controlled (see right panel in figure 1.1). Nevertheless the control of the local density of nucleus is crucial for the performance of single photon experiments [1]. Moreover, also the size of a QD is not controllable, and the emission wavelength strongly depends on it. However, in the last years new techniques have been developed for a better manipulation of the size, density, shape and emission wavelength of quantum dots. Frequent combinations of semiconductor materials used for the fabrication of quantum dots are GaAs/InAs, GaInP/InP and GaN/AlGaN.
There are alternatives to the Stranski-Krastanov growth technique such as the *droplet epitaxy* [15] [16]. This technique has the advantage that it does not require a mismatch between the lattices of the materials involved during the process [17].

Even with droplet epitaxy the position of the quantum dots cannot be controlled. Nevertheless an accurate control over the position of the quantum dot is requested for several applications. Many times is more convenient using other kinds of growing methods, that allow to precisely place a dot in a determined position. When using these methods, the dots are usually called site-controlled quantum dots.

### 1.1.2 Site-controlled Quantum Dots

Several strategies have been developed to obtain a precise positioning of the dots on a semiconductor platform. One common strategy is pre-patterning the semiconductor substrate, drilling holes into it [18]. This can be achieved by using several techniques, such as a combination of *electron beam lithography* and ion etching, by *atomic force nano-lithography* [19], *nanoimprint lithography* [20] or *local oxidation nanolithography* [21]. During the subsequent regrowth and deposition the atoms tends to nucleate in these sites, obtaining regular patterns of Quantum Dots, and control their density as we want (see in Figure 1.2), with a precision of ± 50 nm [1]. The position of quantum dots can also be controlled using masked surfaces and making them grow in the uncovered spots [23].

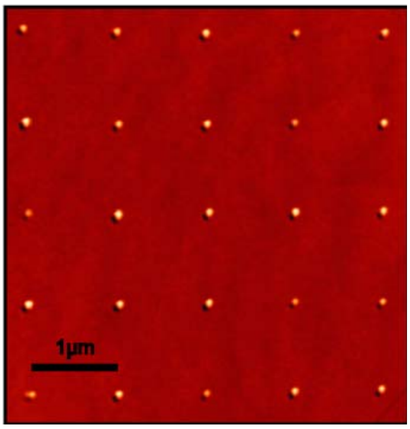

Figure 1.2: Atomic Force Microscope image of site-controlled QDs with 1 $\mu$m lattice period. Image from [22].

During this thesis InAs/GaAs quantum dots embedded in nanowires are used, of the tipology that can be seen in figure 1.3. The nanowires act as waveguides and make the quantum dot emit along the vertical direction. This fact allows a higher photon's collection. However in principle all the measurements shown in this thesis could have been done with a quantum dot not embedded into a photonic structure.

## 1.2 Quantum Dots energy structure

The dimensionality of the system that is considered has strong effects on its energy structure. As can be seen in picture 1.4, depending on how many are the dimensions where there is a quantum confinement of the electrons they have different densities of states. A bulk material has a continuous density of states, depending on the energy as $D(E) \propto \sqrt{E}$.

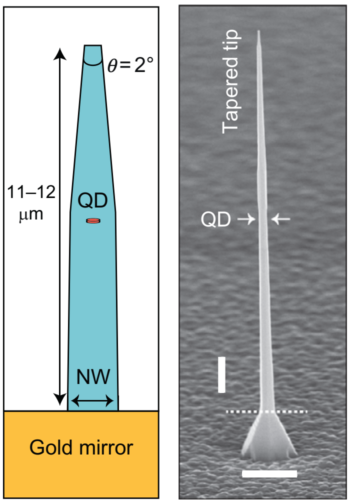
θ=2°
11–12
µm
QD
NW
Gold mirror
Tapered tip
QD → ←

Figure 1.3: Configuration of the type used during this thesis project. The quantum dot of InAs is embedded in a nanowire of GaAs, which acts as a waveguide for the photons, increasing in this way the emission rate along the vertical direction. Image from [24].

However, if the size of one dimension of the material is reduced to nanometric scale (in the order of the De Broglie wavelength) the energies start to be quantized along that direction, hence the density of states changes. In a quantum well the density of states becomes a Heaviside step function, whereas in a quanum wire, as there are two dimensions in which the energies are quantized the density of states depends on the energy as $D(E) = E^{-1/2}$. If the size of the third dimension of our material is reduced, a three dimensional spacial confinement is achieved and the densities become Dirac delta functions. This is what is usually called a quantum dot.

This characteristic gives quantum dots discrete energy states. This is the reason why they are sometimes addressed as "artificial atoms". These energy levels can be partially

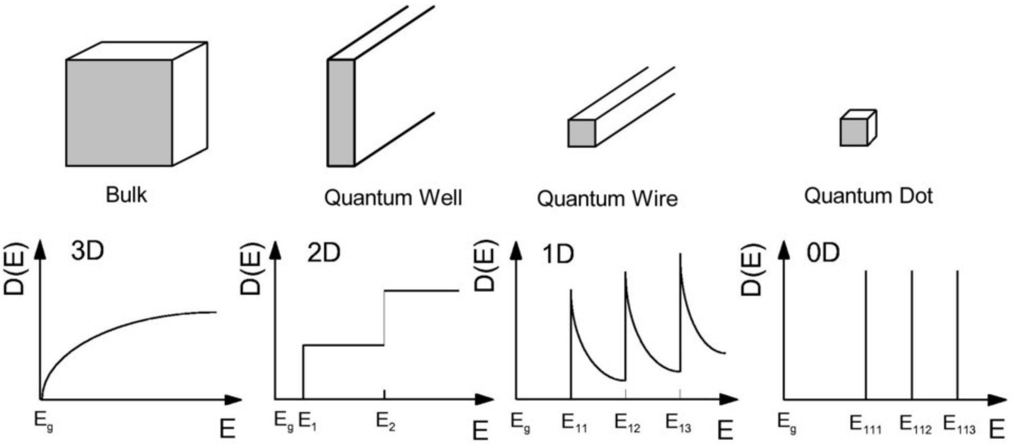
Bulk
Quantum Well
Quantum Wire
Quantum Dot
D(E)
3D
E
E_g
D(E)
2D
E_g E_1
E_2
E
D(E)
1D
E_g
E_11
E_12
E_13
E
D(E)
0D
E_g
E_111
E_112
E_113
E

Figure 1.4: Density of the states as a function of the energy, depending on the system dimension. As we can see, quantum dots have a discrete distribution of states. Image from [25].

controlled modifying various parameters, such as the material of the dot and of the matrix (and consequently the strain between these two materials), the size and the shape of the dot [9].

The evaluation of the energy levels of a quantum dot is difficult to be done analytically, and many numerical models which include various effects (such as the effect of the strain), have been developed. A simpler approach that can be useful to have a qualitative overview about the energy structure of quantum dots consists in using the effective mass approximation [26]. In this approach, a single electron in the conduction band of a semiconductor in a periodic lattice is considered, while the spin is ignored. In a crystal atoms are arranged following a periodic structure, causing a periodic potential

$$V(\mathbf{r}+\mathbf{R}) = V(\mathbf{r}) \tag{1.1}$$

with periodicity equal to

$$\mathbf{R} = n_1\mathbf{a}_1 + n_2\mathbf{a}_2 + n_3\mathbf{a}_3 \tag{1.2}$$

where $\mathbf{R}$ is a generic vector of the Bravais lattice, the $n_i$ are integer numbers and $\mathbf{a}_i$ are the basis vectors describing the unitary cell of the lattice. Due to this periodicity Bloch theorem can be applied, and the wave function can be written as follows:

$$\psi_{\mathbf{k}}(\mathbf{r}) = e^{i\mathbf{k}\cdot\mathbf{r}} u_{\mathbf{k}}(\mathbf{r}) \tag{1.3}$$

where $\mathbf{k}$ is called Bloch wavevector, and $u_{\mathbf{k}}(\mathbf{r})$ is a function with the same periodicity of the potential :

$$u_{\mathbf{k}}(\mathbf{r}+\mathbf{R}) = u_{\mathbf{k}}(\mathbf{r}) \tag{1.4}$$

A single electron in a direct-bandgap semiconductor is considered. Using the effective mass approximation, in a region where the potential varies slowly with respect of the lattice periodicity, the envelope function picture can be used [14][27]. This approach is good when hetero-structures are considered, since the difference between the potentials of the two materials is large, but inside the dot the potential is varies slowly. The wavefunction can be written as

$$\psi(\mathbf{r}) = f(\mathbf{r})u_0(\mathbf{r}) \tag{1.5}$$

where the envelope function satisfies the Schrödinger equation

$$\Big[-\frac{\hbar^2}{2m^*}\nabla^2 + V(\mathbf{r})\Big]f(\mathbf{r}) = Ef(\mathbf{r}) \tag{1.6}$$

When dealing with low-energy states, it is possible to divide the confinement potential into two different components: one in-plane and one perpendicular [28]

$$V(\mathbf{r}) = V_{\perp}(r_{\perp}) + V_{||}(\mathbf{r}_{||}) \tag{1.7}$$

As such, the energy spectrum will be the sum of the energies of these two components. For most of the nanostructures there is a strong confinement along the perpendicular direction (few nanometers) while in the parallel direction the confinement is weaker (usually the horizontal dimensions of quantum dots are bigger than the vertical one) [28]. With this assumption a 2D harmonic potential along the parallel direction and a infinite deep square well along the perpendicular direction can be used.

$$V(\mathbf{r}) = \begin{cases} V(\mathbf{r}) = \frac{1}{2}\omega_0 \mathbf{r}_{\parallel}^2 & |r_{\perp}| < \frac{L}{2} \\ V(\mathbf{r}) = \infty & |r_{\perp}| > \frac{L}{2} \end{cases} \tag{1.8}$$

where L is the vertical size of the quantum dot. With this potential the equation along the two different directions can be factorized and solved for both of them. The resulting energy spectrum can be described as following :

$$E = (n_{\parallel} + 1)\hbar\omega_0 + \Big(\frac{\hbar^2\pi^2}{2m^* L^2}\Big)n_{\perp}^2 \tag{1.9}$$

As can be seen, this energy is the sum of the energies of a 2D harmonic oscillator and a 1D square well potential. Since $L$ is considered small, the spacing between energy states along the vertical direction is large. This model started from the assumption that only low energies are considered, so only the state with $n_{\perp} = 1$ will be occupied.
What we obtain is a spectrum with equally spaced energy states. The wavefunctions that satisfy the equation 1.6 are

$$f(R) \propto H_{n_x}(x)H_{n_y}(y)e^{-\frac{1}{2}\frac{m^*\omega_0}{\hbar}(x^2+y^2)}\cos(\pi z/L) \tag{1.10}$$

where $H_n$ are the Hermite polynomials [29].
The wavefunction for the electrons in the conduction band have an s-like symmetry, hence there is only one conduction band, with spin degeneracy. The wavefunction for the holes in the valence band has p-like symmetry, hence there are three different bands (heavy-hole, light-hole, split-off). Often only the heavy-hole band is considered for the calculations, and the highest valence band state is considered having a heavy-hole nature [7].

The particular choice of the materials used in the quantum dots growth process enables the system to produce transitions only between its states.
If the quantum dot system is cooled down to low temperatures, so that the thermal energy of the whole system is lower than the energy required for the lowest excitation, a quantum dot can be considered as a two-level system [30]. The lowest excited state is the *exciton* state ($X$). An exciton consists in a quasi-particle formed by an electron-hole pair (bound together through Coulomb interaction). This excited state is similar to an hydrogen atom, where the proton is substituted by the hole. This means that also the wavefunction of this bound state is similar to the hydrogen atom one. However, in the exciton, the binding energy between the electron and the hole is smaller than the energy in the hydrogen atom, due to the screening of the other electrons inside the semiconductor. The hole and the electron can have parallel or anti-parallel spin, and their spins are related through exchange interaction [ref]. Considering the spin of the electron on the $z$ axis ($\pm 1/2$) and the spin of the heavy hole ($\pm 3/2$) there are four possibilities for the total angular momentum. If the two spins are anti-parallel ($J_z = \pm 1$), we have a

*bright exciton*, while if they are parallel ($J_z = \pm 2$) we have a *dark exciton* [31]. Only the bright exciton is coupled to light, i.e. recombines emitting a photon, called the exciton photon. The exciton photon is emitted with energy equal to the bangap energy.
An higher excitation process is the *biexciton* ($XX$), where two electrons are excited in the conduction band, with two holes in the valence band. Nevertheless the energy of the biexciton state is usually reduced [32], and it's not twice the energy of the exciton, even if sometimes the opposite situation has been observed [33]. Biexcitons have the interesting property of having the net projection of the angular momentum equal to 0. When more than one electron is excited to the conduction band, the recombination processes involve photons emitted in a cascade. This means that if the system is excited to the biexciton state, during the recombination the biexciton photon associated to the transition $|XX\rangle \rightarrow |X\rangle$ will be first emitted, and subsequently will be emitted the exciton photon, correspondent to the transition $|X\rangle \rightarrow |gs\rangle$, where $|gs\rangle$ is the ground state.
There are also other excited states, such as *trions* ($X^+$ or $X^-$), i.e. charged excitons. A schematic illustration of these states is shown in figure 1.5.

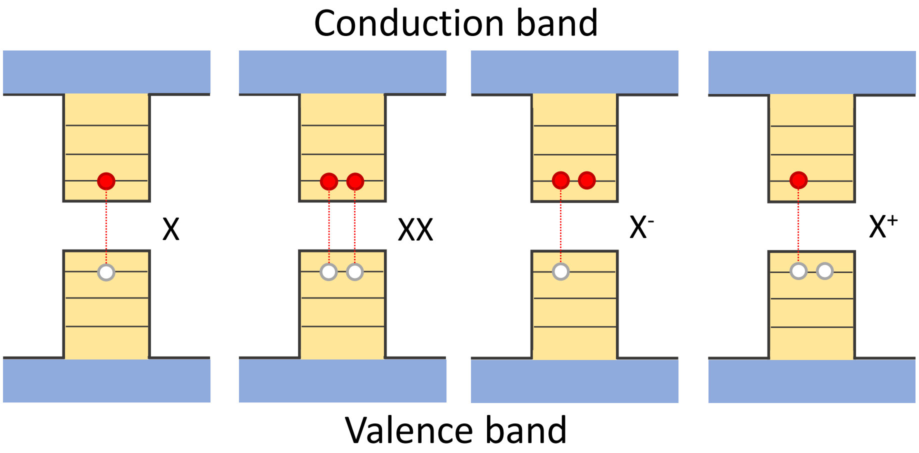

Figure 1.5: Schematics of some bound states in a quantum dot. From left to right : an exciton (X), a biexciton (XX), a negative trion (X$^-$), a positive trion (X$^+$).

As quantum dots show discrete energy levels, their emission spectra have discrete emission lines, where their wavelengths are equal to the energy transition between the states. As the time evolution of a state population follows an exponential law

$$N(t) = N_0 e^{-\frac{t}{\tau}} \tag{1.11}$$

(where $\tau$ corresponds to the mean life time of a state), the emission line as function of the emission energy follows a Lorentzian curve,

$$I(\epsilon) = \frac{I_0 \Gamma^2/4}{(\epsilon - E_{ba})^2 + \Gamma^2/4} \tag{1.12}$$

where $E_{ba}$ is the energy difference between the states b and a, and the broadness of the curve depends on $\Gamma = \hbar/\tau$. This is known as natural broadening of the line. When is only present this factor the emitted photons are called Fourier transform-limited photons.

However, there are other factors that make the emission lines broader. In the specific case of a quantum dot, the interactions between the dot and the matrix causes fluctuations of the energy levels of the dot, which reduce the lifetime of the state and then make the emission line broader.
Depending on the geometry of the QD the harmonic potential along the x-y direction can be asymmetric. This asymmetry causes a fine structure splitting of its emission spectrum [34]. In this case the exciton line is split into two orthogonal, linearly-polarized components [35]. This splitting can be an obstacle if the indistinguishability between two photons emitted during the cascade is needed. In fact, in this case different transition can occur during recombination process, between different energy levels (Figure 1.6). However, if the splitting is smaller than the exciton linewidth, quantum dots can still be used as sources of entangled photons. When there is no fine splitting of the energy levels, the dot is called *degenerate quantum dot*, and the emitted photons show circular polarization.

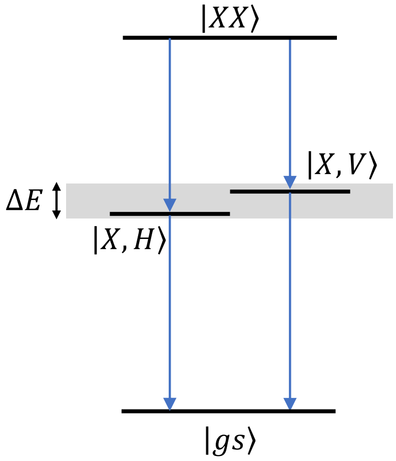

Figure 1.6: Illustration of the energy splitting of the exciton, due to the asymmetry of the harmonic potential along the x-y direction. The two exciton photons are emitted with perpendicular polarizations. If the energy splitting is smaller than the energy fluctuation of the level ($\Delta E$), the quantum dot can still be used as a source of entangled photons.

## 1.3 Excitation of a QD

As previously said, once the thermal energy is below the energy needed for the lowest energy transition between the valence band and the conduction band of the quantum dot, it can be treated as a two-level system. The QD can be optically excited using a laser and make it emit single photons. There are two types of excitation schemes for single-photons generation in QDs:

- above band excitation;
- resonant excitation;

### 1.3.1 Above band excitations

The simplest excitation scheme is the above band excitation. This excitation can be conducted in two different ways, as seen in figure 1.7. In the first one the system can be excited using a laser light with a higher energy than the bandgap of the quantum dot and the wetting layer, exciting the electrons in the conduction band of the substrate. Since the transitions of an InAs/GaAs quantum dot are usually around 900 nm, a 635 nm wavelength laser can be used. The second procedure consists in the wetting layer excitation. In this case the electrons are excited to the wetting layer conduction band, which has an energy between the bandgap of the matrix and the bandgap of the quantum dot.

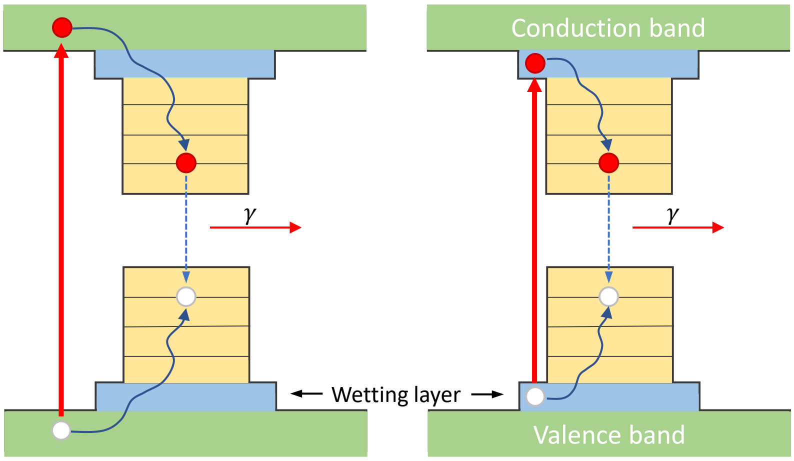

Figure 1.7: Schematics of the above band excitation schemes. On the left: excitation in the matrix bandgap. On the right: wetting layer excitation.

In both cases, the laser excitation promotes the electrons in one of these two conduction bands, producing an electron-hole couple. These carriers can be probabilistically captured inside the quantum dot conduction band with subsequent relaxation to its ground state (s-shell) through phonons scattering [36]. Then they recombine emitting a photon. Since in wetting layer excitation there is less phonon scattering, it shows less background noise than the excitation in the substrate conduction band. These phonon interactions cause an asymmetric broadening of the emission lines. [37].

In order to understand how the carriers will populate the excited states a simplified model of a multi-level system can be considered. Only the transition between close levels are allowed, and only neutral states are considered. $P_n$ is the occupation probability of the state with $n$ excited electrons, $r$ the excitation rate and $\gamma$ the de-excitation rate. Then the time variation of the population of the state with $n$ excited electron will have a negative term

$$\frac{dP_n}{dt} = -rP_n - n\gamma P_n \tag{1.13}$$

where the first term on the right side is due to the excitation of one electron to the state $P_{n+1}$, while the second term is due to the de-excitation to the state $P_{n-1}$. In fact each electron in the state have a decay rate $\gamma$, and in a state with $n$ electrons we will have a

total decay rate equal to $n\gamma$.
On the other hand side the state will gain particles from the de-excitation of the $P_{n+1}$ state and prom the excitation of the $P_{n-1}$ state, so the number of particles will increase of

$$\frac{dP_n}{dt} = rP_{n-1} + (n+1)\gamma P_{n+1} \tag{1.14}$$

The total time variation of the population of state $P_n$ will be

$$\frac{dP_n}{dt} = -(r + n\gamma)P_n + rP_{n-1} + (n+1)\gamma P_{n+1} \tag{1.15}$$

If the $P_n$ state is considered constant in time

$$\frac{dP_n}{dt} = 0 \tag{1.16}$$

the equation becomes the following :

$$0 = -(r + n\gamma)P_n + rP_{n-1} + (n+1)\gamma \tag{1.17}$$

and, substituting in this equation the subsequent expression for $P_n$:

$$P_n = \left(\frac{r}{\gamma}\right)^n \frac{1}{n!} e^{-\frac{r}{\gamma}} = \frac{\mu^n}{n!} e^{-\mu} \tag{1.18}$$

the identity $0 = 0$ is obtained. This means that this is a solution of this differential equation [?]. $\mu$ is called the mean number of excitations. In fact, when estimating the mean of the distribution :

$$\begin{aligned}\sum_{n=1}^{\infty} nP_n &= \sum_{n=1}^{\infty} n\left(\frac{r}{\gamma}\right)^n \frac{1}{n!} e^{-\frac{r}{\gamma}} = \\ &= \frac{r}{\gamma} e^{-\frac{r}{\gamma}} \sum_{n=1}^{\infty} \left(\frac{r}{\gamma}\right)^{(n-1)} \frac{1}{(n-1)!} = \\ &= \frac{r}{\gamma} e^{-\frac{r}{\gamma}} \sum_{n=0}^{\infty} \left(\frac{r}{\gamma}\right)^n \frac{1}{n!} = \frac{r}{\gamma} e^{-\frac{r}{\gamma}} e^{\frac{r}{\gamma}} = \frac{r}{\gamma} = \mu\end{aligned} \tag{1.19}$$

The mean of the distribution is equal to $\mu$. The equation 1.18 a Poissonian distribution, with mean equal to $\mu$. $\mu$ is proportional to the excitation power, $\mu = cP$. In fact the power of the beam used to excite the system is related to the number of photons that are sent on it, and the more photons are sent, the more electrons will be excited.
What obtained tells that the probability of exciting n electrons at the same time under above excitation follows a Poissonian distribution. Experimentally it's not possible to measure the occupation probability of a state, but its decay rate can be measured. In fact the decay rate of a state with $n$ excited particles is equal to

$$R_n = n\gamma P_n \tag{1.20}$$

If we substitute $n = 1$ the decay rate of a state with one excited particle, i.e. the decay rate of the exciton, is obtained:

$$R_{\mathrm{X}}(\mu) = \gamma\mu e^{-\mu} \tag{1.21}$$

While for $n = 2$ we have the probability of having a biexciton:

$$R_{\mathrm{XX}}(\mu) = \gamma\mu^2 e^{-\mu} \tag{1.22}$$

In figure 1.8 $P_n$ versus the excitation power is plotted. As can be seen, different excitation processes shows different slopes. Moreover, when the mean number of excitations $\mu$ reaches a value close to one, the probability sharply drops to zero. Unfortunately this behaviour cannot be seen experimentally because if the excitation power is too high, a broadband emission dominates the spectrum, covering the lines under consideration [14]. Above band excitation is easy to obtain, since all is needed is a laser with a higher energy

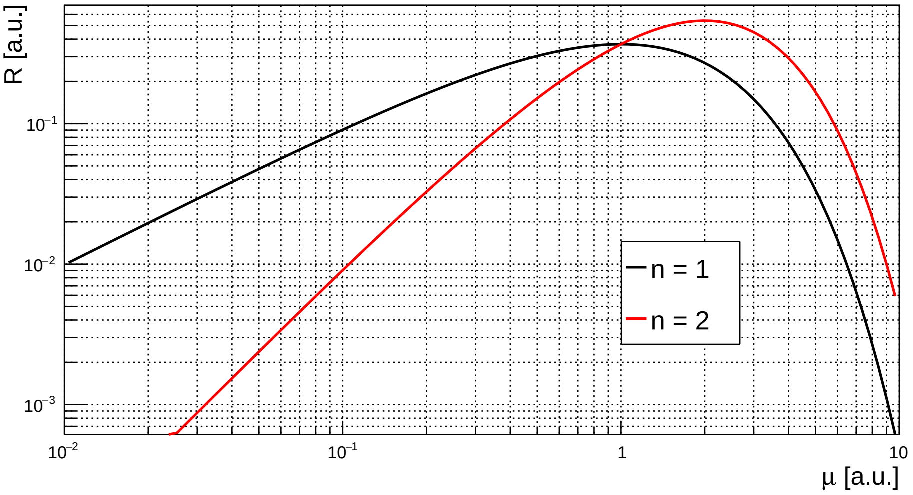

Figure 1.8: Graphic of the emission rate $R_n$, from equation 1.15, as function of the mean number of excitations.

than the matrix bandgap. Moreover it is quite efficient, and even with a small power it is possible to excite many carriers to the conduction band, and then produce a good amount of photons. Since the excitation energy is different from the one of the emitted photons, they show different wavelengths and it is easy to discriminate the two sources of light. Finally, since as can be seen in figure 1.8 different excited states show different behaviours when the excitation power is increased, above excitation can be also useful to discriminate different excitation processes.

On the other hand, there are complication related to various reasons. For example, the non- radiative relaxation processes introduce time jitter in the generation of photons, which reduces their indistinguishability [38]. Moreover there are problems related to the probabilistic natures of the capturing process, the probabilistic occupation of excited states and the relaxation to the s-shell through phonon scattering. All these factors cause dephasing, which reduces the coherence length of the emitted photons, that is also crucial for obtaining a good indistinguishability between the photons. These bad properties make the photons emitted after an above band excitation unsuitable for several applications, like quantum information protocols [39].

### 1.3.2 Resonant excitations

A way to obtain a better controlled population of the excited states is using the resonant excitations. This kind of excitations can be obtained following two different approaches, the in-band quasi-resonant excitation and the in-band resonant excitation.

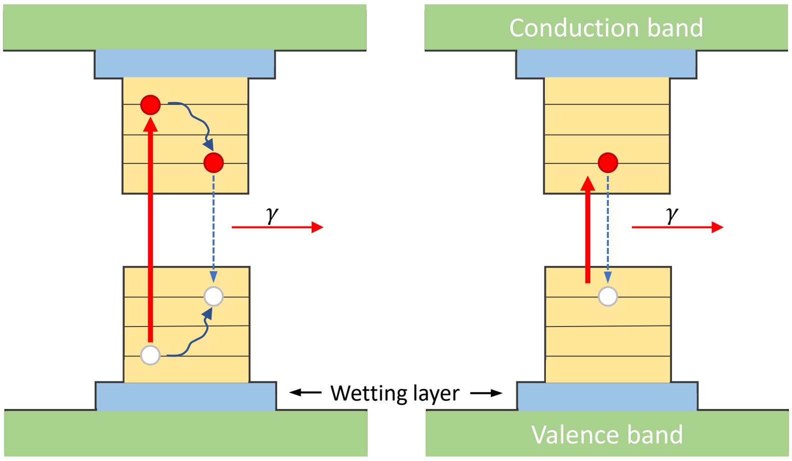

Figure 1.9: Schematics of the in-band excitation schemes. On the left: quasi-resonant excitation. On the right: resonant excitation.

When a quantum dot is excited with a in-band quasi-resonant excitation (also called p-shell excitation) (figure 1.9, left), an electron is excited to the p-shell of the quantum dot conduction band. Then this electron relaxes to the s-shell through phonon scattering and recombines to the ground state emitting a photon. Usually the relaxation takes place in few picoseconds [40]. This fact reduces the time jitter in the emission. Since the relaxation happens with less phonon scattering than in the case of the above band excitations, there is less dephasing from this source and the emitted photons have a longer coherence length.

However this excitation scheme can't compete with the pure resonant excitation (figure 1.9, right). With this excitation one electron is excited to the s-shell of the conduction band, and it directly recombines to the ground state emitting a photon with energy equal to the energy of the bandgap. Since in this scheme no relaxation processes through phonon interaction are involved, with this kind of excitation several dephasing processes can be avoided. Moreover, there is not a time jitter related to the emission time of the photon after the excitation. Also this factor reduces dephasing, and allows to create single photons on demand.

The emitted photons will have then a longer coherence length. On the other hand, in order to get this excitation a laser with exactly the wavelength corresponding to the transition to the s-shell is needed. This means that it's harder to discriminate the two sources of light (the laser and the quantum dot). To solve the problem, usually the sample is excited by the side, while the emission is perpendicular. Another option is to use a collinear excitation, i.e. the excitation light and the emitted light follow the same path. In this case the two lights, the one from the laser and the one from the quantum dot, are divided into two different paths. As said before, realizing a resonant excitation is challenging but has many advantages, such as better properties of the emitted photons. Another important property of the resonant excitation is that allows the deterministic creation of a population in excited state. In order to create the inversion of the population a pulsed laser is needed. In fact under resonant $\pi$ pulses (pulses with the area equal to $\pi$) the system can be deterministically excited in the exciton state. The *Rabi oscillations* are then observed [41], which can be seen in figure 1.10. Here the probability of finding the system in the excited state depends on time, and oscillates with frequency $\Omega$, called Rabi frequency. If the light pulse is detuned from the frequency of the transition the population oscillates at the *generalized Rabi frequency* $\tilde{\Omega}$, which depends on the detuning in the subsequent way

$$\tilde{\Omega}(\omega) = \sqrt{|\Omega|^2 + \Delta^2} \tag{1.23}$$

where $\Delta = \omega - \omega_{ab}$ is the difference between the laser frequency and the transition

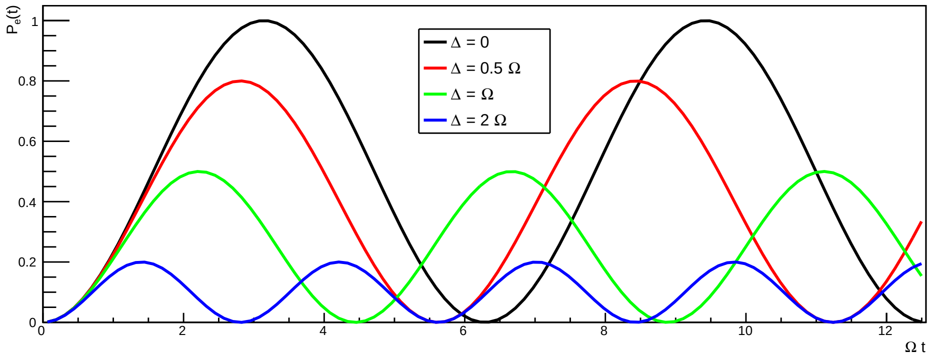

Figure 1.10: Plot of the probability of finding the system in the excited state, as function of time, for different detunings. As can be seen, when the detuning is different from zero the probability of having the system in the excited state oscillates with a different frequency, and becomes lower than 1.

frequency of the two levels of the system ($\omega_{ab}$). The probability to find the system in the excited state is [42]

$$P_e(t) = \frac{\Omega^2}{\tilde{\Omega}^2}\left(\frac{1}{2} - \frac{1}{2}\cos(\tilde{\Omega}t)\right) \tag{1.24}$$

When the laser is detuned from the transition frequency, the probability of bringing the system to the excited level becomes lower than 1. Experimentally the resonant excitation can be observed looking at the intensity of the considered emission line for different lengths of the excitation pulses.

Another kind of resonant excitation is the *two-photon excitation*. Due to the optical selection rules, it is impossible to excite from the ground state to the biexciton state using only one resonant photon. With this excitation scheme two photons with energy equal to half the energy gap between the ground state and the biexciton state are sent on the quantum dot at the same time. In this way, exploiting a virtual level between the two states, it is possible to excite the quantum dot directly on the biexciton state (as can be seen in figure 1.11). Afterwards the excited state recombines to the ground state emitting photons in a cascade via the exciton level. As previously said, if there is an asymmetry in the harmonic potential which confines electrons in the dot, two different paths can occur, where the emitted photons have perpendicular polarizations. This method is useful when the splitting is smaller than the linewidth of the exciton state, in fact in this way the two paths become indistinguishable, and it emits a pair of polarization-entangled photons. With this method is also easier to separate the laser light from the emission of the quantum dot, in fact since the wavelengths are different, only a spectral filter is needed.

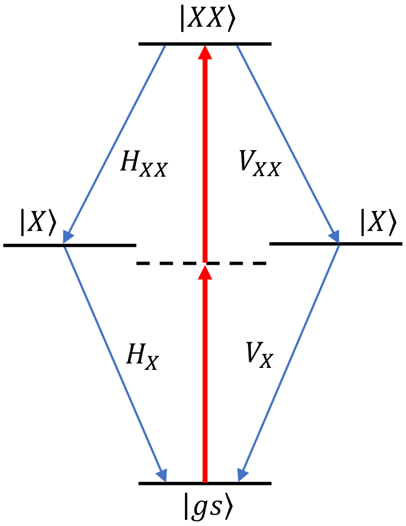

Figure 1.11: Schematics of the two-photon resonant excitation scheme. The system is excited with one photon to virtual energy level between the ground state and the biexciton level. The second photon excite the system from the virtual to the biexciton level. Then photons are emitted in a cascade. If the energy splitting of the exciton level is smaller than the emission line bandwidth, this excitation scheme can be used to obtain pair of polarization-entangled photons.

## 1.4 Photon statistics

As pointed out in appendix A, Fock states are the eigenvalues of the number operator, but not of the Hamiltonian of the electromagnetic field. Coherent states (*Glauber states*) are the best representation of a classical electromagnetic field in the quantum mechanical description. The light emitted by a laser operated above its threshold is in a coherent state $|\alpha\rangle$. Coherent states are the eigenstates of the annihilation operator:

$$\hat{a}\,|\alpha\rangle = \alpha\,|\alpha\rangle \tag{1.25}$$

the complex number $\alpha = |\alpha|\exp(i\alpha)$ is the complex amplitude of an electromagnetic wave, and $|\alpha|^2 = \langle\alpha|\hat{n}|\alpha\rangle = N$ is the expectation value of the photon number operator

$|n\rangle$ [43]. A coherent state has a not fixed number of photons, and can be expressed in terms of Fock states as

$$|\alpha\rangle = e^{-\frac{|\alpha|^2}{2}} \sum_{n=0}^{\infty} \frac{\alpha^n}{\sqrt{n!}} |n\rangle \tag{1.26}$$

The probability of finding n photons in this coherent state, with the mean number of photons equal to $\alpha^2 = \bar{N}$ is given by [43]

$$P_\alpha(n) = |\langle n|\alpha\rangle|^2 = \frac{\bar{N}^n}{n!} e^{-\bar{N}} \tag{1.27}$$

This probability is then a Poissonian distribution, with mean and variance equal to N. This means that the light emitted by a laser follows this distribution, and since it is Poissonian the more the distribution mean is increased, the more this distribution will assume a gaussian shape. A distribution with the same mean but with bigger variance is called *Super-Poissonian.* Respectively, a distribution with a smaller variance is called *Sub-Poissonian.*

Having the system prepared in a Fock state $|n\rangle$ is considerably different than having it in a coherent state $|\alpha\rangle$. In fact if a coherent state is considered and the mean number of photons of the distribution is equal to 1, the probability of detecting one photon when a measurement is made is not equal to 1, but, according to the Poissonian distribution, $P_\alpha(1) = 0.366$. On the other hand, having a Fock state $|n\rangle$ means that when a measurement is made the probability of detecting $n$ photons is exactly equal to 1. This difference is important, because it is easy to understand that with a single photon source single photons can be deterministically produced.

Light emitted by classical light sources, i.e. a spectral lamp, is incoherent and follows a Super-Poissonian distribution. A characteristic of this kind of light is that if the time of arrival on a sensor of the photons emitted by this source is measured, it will be observed that they arrive in groups: this is called as *photon bunching.* Since a Poissonian distribution describes random events, a laser source emits photons randomly in the time domain. The light emitted by a single photon source follows a Sub-Poissonian distribution. The relative associated state to this distribution is a Fock state $|n\rangle$. With a single-photon source only one photon is emitted at a time, so if their arrival time is observed it can be noticed that they are more equally spaced than in the other two cases. This phenomenon is called *photon antibunching.* A clear sketch of these three cases can be seen in the Figure 1.12.

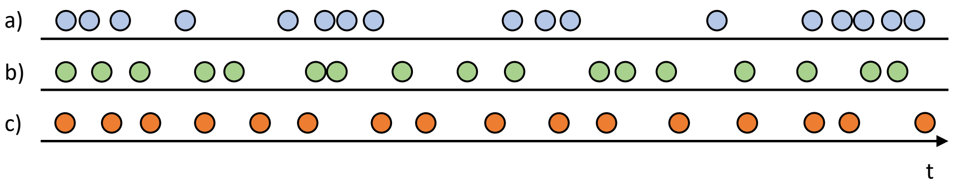

Figure 1.12: Photon time distribution for different types of sources: a) super Poissonian (bunching), b) Poissonian (random), c) sub Poissonian (antibunching).

A quantum dot is a single-photon source, so the emitted photons follow a Sub-Poissonian statistic and show the antibunching. Remembering what was said in section 1.2, quantum dots can be seen as a two-level system. From this point of view it is easy to understand the antibunching : every excited state has its own finite lifetime, so when the excited state de-excites to ground state and emits a photon, in order to have another photon it must be excited again, and it must relax again to the ground state. Since every excited state has its proper lifetime, there is a dead time before the emission of two subsequent photons.

This property is really useful for all quantum photonics, in fact it means that with a single photon source there is the possibility to produce single photons on demand.

Antibunching is thus a peculiar characteristic of single photon sources, and it can be measured to estimate the quality of the source as a single photon emitter. Usually this quantity is measured with the *second-order correlation function* $g^{(2)}(\tau)$, which is defined for a classical electric field as [44]

$$g^{(2)}(\mathbf{r}_1, t_1; \mathbf{r}_2, t_2) = \frac{\langle \mathbf{E}^*(\mathbf{r}_1, t_1)\mathbf{E}^*(\mathbf{r}_2, t_2)\mathbf{E}(\mathbf{r}_1, t_1)\mathbf{E}(\mathbf{r}_2, t_2)\rangle}{\langle |\mathbf{E}(\mathbf{r}_1, t_1)|^2\rangle \langle |\mathbf{E}(\mathbf{r}_2, t_2)|^2\rangle} \tag{1.28}$$

where $\langle\cdot\rangle$ is a ensamble average. When dealing with stationary states, this average can be replaced with a time average, calculated as

$$\langle \mathbf{E}^*(\mathbf{r}_1, t_1)\mathbf{E}(\mathbf{r}_1, t_1)\rangle = \frac{1}{T}\int_0^T \mathbf{E}^*(\mathbf{r}_1, t_1)\mathbf{E}(\mathbf{r}_1, t_1)\mathrm{dt}_1 \tag{1.29}$$

and $T$ is bigger than the characteristic oscillation time of the electric field. With plane parallel waves $\mathbf{r} = z$. Moreover only stationary states are considered, therefore the function will not depend anymore on the time, but on the time difference $\tau = t_2 - t_1$. Since the intensity is defined as the square modulus of the electric field $g^{(2)}(\tau)$ can be written as function of the intensity. :

$$g^{(2)}(\tau) = \frac{\langle I(t)I(t+\tau)\rangle}{\langle I(t)\rangle \langle I(t)\rangle} \tag{1.30}$$

When the field is quantized, it is substituted with the correspondent operator:

$$\mathbf{E} \to \hat{E}^+ \qquad \mathbf{E}^* \to \hat{E}^- \tag{1.31}$$

where

$$\hat{E}^+(\mathbf{r}, t) = i\sqrt{\frac{\hbar\omega}{2\epsilon_0 V}}\hat{a}e^{i(\mathbf{k}\cdot\mathbf{r}-\omega t)} \tag{1.32}$$

$$\hat{E}^-(\mathbf{r}, t) = -i\sqrt{\frac{\hbar\omega}{2\epsilon_0 V}}\hat{a}^\dagger e^{-i(\mathbf{k}\cdot\mathbf{r}-\omega t)} \tag{1.33}$$

and the second order correlation function can be written as function of the annihilation and creation operators:

$$g^{(2)}(\tau) = \frac{\langle \hat{a}^\dagger(t)\hat{a}^\dagger(t+\tau)\hat{a}(t)\hat{a}(t+\tau)\rangle}{\langle \hat{a}^\dagger(t)\hat{a}(t)\rangle^2} \tag{1.34}$$

where $\hat{a}$ and $\hat{a}^\dagger$ are the annihilation and creation operators. When the second order correlation function is calculated at $t = 0$ the commutation rule $[\hat{a}, \hat{a}^\dagger] = 1$ can be used and $g^{(2)}(0)$ can be written as

$$g^{(2)}(0) = \frac{\langle \hat{N}(\hat{N} - 1) \rangle}{\langle \hat{N} \rangle^2} \tag{1.35}$$

where $\hat{N}$ is the number operator. Using the density matrix $\hat{\rho}$ this value can be explicitly calculated. The density matrix is defined as

$$\hat{\rho} = \sum_j P_j \left| \psi_j \right\rangle \left\langle \psi_j \right| \tag{1.36}$$

In fact, given an observable $\hat{O}$ its average value is calculated as

$$\begin{aligned} \langle O \rangle &= \sum_j P_j \langle \psi_j | \hat{O} | \psi_j \rangle = \sum_j P_j \mathrm{Tr}(\left| \psi_j \right\rangle \left\langle \psi_j \right| \hat{O}) = \\ &= \mathrm{Tr}\Big( \sum_j P_j \left| \psi_j \right\rangle \left\langle \psi_j \right| \hat{O} \Big) = \mathrm{Tr}(\hat{\rho}\hat{O}) \end{aligned} \tag{1.37}$$

The value of $g^{(2)}(0)$ is calculated as

$$\begin{aligned} g^{(2)}(0) &= \frac{\langle \hat{N}(\hat{N} - 1) \rangle}{\langle \hat{N} \rangle^2} = \frac{\mathrm{Tr}(\hat{\rho}\hat{N}(\hat{N} - 1))}{(\mathrm{Tr}(\hat{\rho}\hat{N}))^2} = \\ &= \frac{\sum_{n=0}^{\infty} P_n \langle n | \hat{N}(\hat{N} - 1) | n \rangle}{\Big( \sum_{n=0}^{\infty} P_n \langle n | \hat{N} | n \rangle \Big)^2} = \frac{\sum_{n=0}^{\infty} P_n n(n - 1) \langle n | n \rangle}{\Big( \sum_{n=0}^{\infty} n P_n \langle n | n \rangle \Big)^2} = \\ &= \frac{2P_2 + 6P_3 + 12P_4 + 20P_5 + \ldots}{\bar{N}^2} \end{aligned} \tag{1.38}$$

$g^{(2)}(\tau)$ is essentially the probability of detecting a photon after a time delay $\tau$ when a photon is detected at $t = 0$. For sources that emit photons with different statistics $g^{(2)}(0)$ will assume different values. For a single photon source $P_1 = 1$, so $g^{(2)}(0) = 0$ and the antibunching can be seen. For a Poissonian source $g^{(2)}(0) = 1$ and the photons are uncorrelated, while for a super-Poissonian source $1 < g^{(2)}(0) < 2$ and the photons show bunching. These three cases can be seen in picture 1.13. Since the coherent states are the link between the classical electric field and the quantum electric field (because we have $\langle \alpha | \hat{E}(\mathbf{r}, t) | \alpha \rangle = \mathbf{E}(\mathbf{r}, t)$, as can be seen in appendix A), if a value $g^{(2)}(0) < 1$ is observed, it is possible to affirm that the considered source is a non-classical light emitter.

Experimentally these different behaviours related to different kind of sources can be observed with an *Hanbury-Brown-Twiss* setup, which consists essentially of a 50:50 beam splitter, and two *Avalanche Photodiodes* (APDs). A scheme of this setup is shown in figure 1.14. A light beam is sent through this beam splitter, and the two out coming beams are sent on the two APDs. The signals are then directed to a time to amplitude converter (TAC). A Time To Amplitude converter is a device that converts a time interval into a voltage, that increases linearly as the time increases.

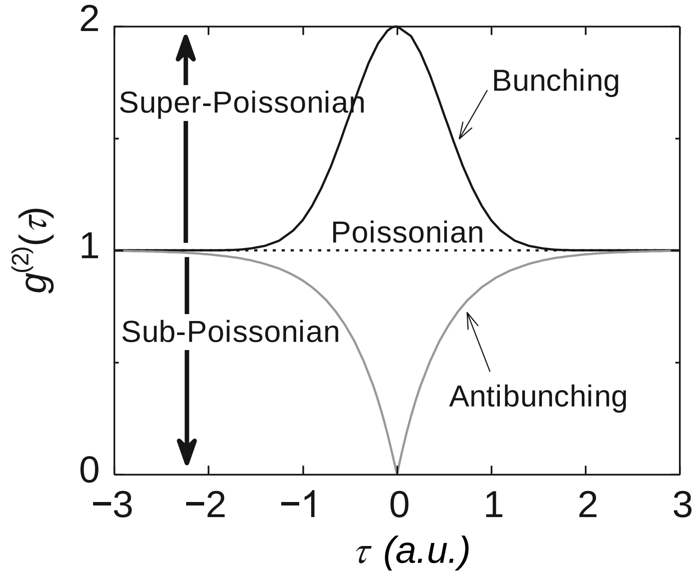

Figure 1.13: Second order correlation function $g^{(2)}(\tau)$ for different kind of sources. Image from [45].

The first signal coming from one of this detectors is the start of this module, while the signal of the other detector is the stop. The resulting plot is a histogram with the number of photon pairs as function of the delay time between the two signals.

This measurement can be done to observe the autocorrelation between two exciton photons, two biexcion photons, or the cross-correlation between an exciton and a biexciton photon. Typical results of these measurements for continuous and pulsed excitations are shown in figure 1.15. As can be seen, for continuous wave sources the correlation between excitons shows a dip when close to $\tau = 0$. In the same way using a pulsed source the peak at $\tau = 0$ vanishes. The other peaks are due to the use of a pulsed excitation light with a certain repetition rate.

## 1.5 Photons indistinguishability

In quantum photonics one crucial property is the indistinguishability of the photons. While in classical mechanics two different entities are always distinguishable, in quantum mechanics identical states are always indistinguishable.

Two photons are perfectly indistinguishable if their density matrices $\hat{\rho}_1$ and $\hat{\rho}_2$ are the same. The indistinguishability between two sources is defined as

$$\mathcal{I} = 1 - \frac{1}{2}||\hat{\rho}_1 - \hat{\rho}_2||^2 \tag{1.39}$$

The difference between the two density matrices is equal to 0 when they describe exactly the same state. The perfect indistinguishability is hence reached when $\mathcal{I} = 1$, while when it is equal to 0 the sources are perfectly distinguishable. If each source is in a pure state

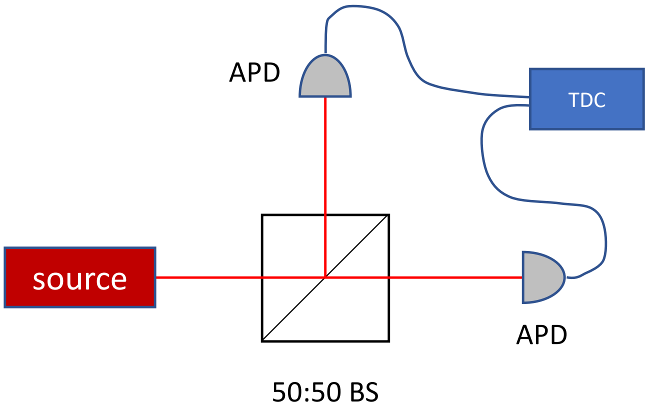

Figure 1.14: Schematics of the experimental setup used for a Hanbury-Brown-Twiss measurement. A beam is sent through a 50:50 beam splitter. The two out coming beams are sent in two different APDs. The first signal starts a clock and the second signal stops it. The two signals are sent into a Time To Digital Converter and the time difference between the two signals is recorded.

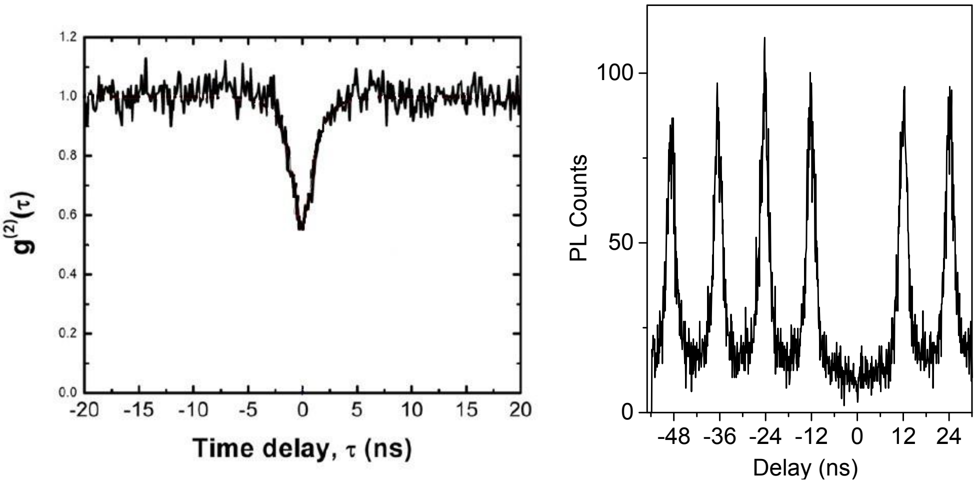

Figure 1.15: Second order correlation function $g^{(2)}(\tau)$ for different kind of excitation. Left: under above band continuous excitation. Right: under above band pulsed excitation.

the density matrices are equal to

$$\hat{\rho}_1 = |\psi_1\rangle \langle\psi_1| \qquad \hat{\rho}_2 = |\psi_2\rangle \langle\psi_2| \tag{1.40}$$

and the indistinguishability can be calculated as [46]

$$\mathcal{I}(\hat{\rho}_1, \hat{\rho}_2) = |\langle\psi_1|\psi_2\rangle|^2 \tag{1.41}$$

In principle the indistinguishability can be calculated by measuring all the quantum properties of the two states, like the polarization state, or the spectral, spacial and temporal profiles. Experimentally the indistinguishability between two different sources is measured with the Hong-Hou-Mandel (HOM) interference [47], that is realized sending onto a 50:50 beamsplitter two photons at the same time. According to quantum mechanics, since photons follow Bose-Einstein statistics, when they are perfectly indistinguishable and are sent on a beamsplitter, they always go out coupled.

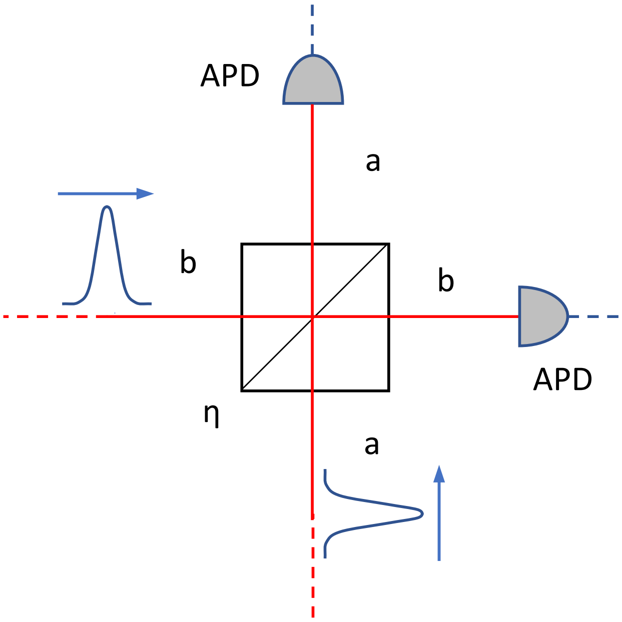

Figure 1.16: Illustration of the experimental setup for the Hong-Ou-Mandel interference. Two photons are sent on a 50:50 beamsplitter, and the outcoming signal is sent into two APDs. These signals are sent then on a coincidence counter.

Let's consider a two photon interference: the initial state of the system is [48]

$$|\psi_{\text{in}}\rangle_{ab} = \hat{a}_j^\dagger \hat{b}_k^\dagger |0\rangle_{ab} = |1;j\rangle_a |1;k\rangle_b \tag{1.42}$$

where $\hat{a}^\dagger$ and $\hat{b}^\dagger$ are bosonic creations operators related to the two different ways photons can enter in a beamsplitter, while $j$ and $k$ are some properties of the two photons that make them distinguishable, like the polarization. So far no assumptions about the distinguishability of the two photons. The situation can be seen in figure 1.16.

A beam splitter with reflectivity $\eta$ can be represented in a quantum mechanical point of view as an unitary operator $\hat{U}_{BS}$ that acts on the creations operators in the following way [44]

$$\hat{a}_j^\dagger \xrightarrow{\hat{U}_{BS}} \sqrt{1-\eta}\,\hat{a}_j^\dagger + \sqrt{\eta}\,\hat{b}_j^\dagger \tag{1.43}$$

$$\hat{b}_k^\dagger \xrightarrow{\hat{U}_{BS}} \sqrt{\eta}\,\hat{a}_k^\dagger - \sqrt{1-\eta}\,\hat{b}_k^\dagger \tag{1.44}$$

Where the minus sign is due to the fact that $\hat{U}_{BS}$ is an unitary operator. Applying this operator to the initial state $|\psi_{in}\rangle_{ab}$ the final state is:

$$\begin{aligned} |\psi_{\text{out}}\rangle_{ab} &= \hat{U}_{BS}\,|\psi_{in}\rangle_{ab} = \hat{U}_{BS}\,\hat{a}_j^\dagger\,\hat{b}_k^\dagger\,|0\rangle_{ab} = \\ &= \big(\sqrt{1-\eta}\,\hat{a}_j^\dagger + \eta\,\hat{b}_j^\dagger\big)\big(\sqrt{\eta}\,\hat{a}_k^\dagger - \sqrt{1-\eta}\,\hat{b}^\dagger\big)\,|0\rangle_{ab} = \\ &= \big(\sqrt{\eta(1-\eta)}\,\hat{a}_j^\dagger\hat{a}_k^\dagger - (1-\eta)\,\hat{a}_j^\dagger\hat{b}_k^\dagger - \sqrt{\eta(1-\eta)}\,\hat{b}_j^\dagger\hat{b}_k^\dagger + \eta\,\hat{b}_j^\dagger\hat{a}_k^\dagger\big)\,|0\rangle_{ab} \end{aligned} \tag{1.45}$$

If $\eta = 1/2$ the result is

$$|\psi_{\text{out}}\rangle_{ab} = \frac{1}{2}\big(\hat{a}_j^\dagger\hat{a}_k^\dagger - \hat{a}_j^\dagger\hat{b}_k^\dagger + \hat{b}_j^\dagger\hat{a}_k^\dagger - \hat{b}_j^\dagger\hat{b}_k^\dagger\big)\,|0\rangle_{ab} \tag{1.46}$$

The figure 1.17 shows the four different terms of the equation. As said before, when Hong-Ou-Mandel interference is made, the number of coincidence counts from the two APDs is important. The probability of detecting two photons at the same time is related to their distinguishability. For example, the polarization distinguishability can be considered.

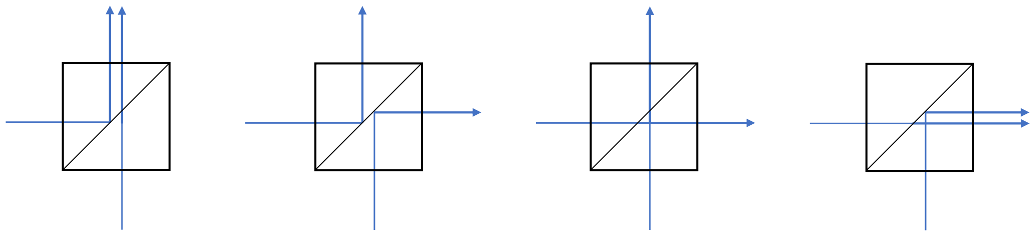

Figure 1.17: Schematics that shows the different ways two photons can interact with a beamsplitter. These terms are written in equation 1.46.

A photon can have a vertical (V) or horizontal (H) polarization, or a linear combination of them, $\alpha V + \beta H$, where $\alpha^2 + \beta^2 = 1$.
If two photons with different polarizations are sent on the beamsplitter, the output state will be

$$\begin{aligned} |\psi_{\text{out}}\rangle_{ab} &= \frac{1}{2}\big(\hat{a}_H^\dagger\hat{a}_V^\dagger - \hat{a}_H^\dagger\hat{b}_V^\dagger + \hat{b}_H^\dagger\hat{a}_V^\dagger - \hat{b}_H^\dagger\hat{b}_V^\dagger\big)\,|0\rangle_{ab} = \\ &= \frac{1}{2}\big(\,|1;H\rangle_a\,|1;V\rangle_a - |1;H\rangle_a\,|1;V\rangle_b + |1;H\rangle_b\,|1;V\rangle_a - |1;H\rangle_b\,|1;V\rangle_b\,\big) \end{aligned} \tag{1.47}$$

In this case all the four possibilities shown in figure 1.17 are still present in the output state. This means that the probability of having a coincidence count, i.e. outcoming photons in the two different output ports, will be equal to 1/2.
When two photons with same polarization are considered (e.g. vertical polarization), the

final state will be

$$\begin{aligned}|\psi_{\text{out}}\rangle_{ab} &= \left(\hat{a}^\dagger_V\hat{a}^\dagger_V - \cancel{\hat{a}^\dagger_V\hat{b}^\dagger_V} + \cancel{\hat{b}^\dagger_V\hat{a}^\dagger_V} - \hat{b}^\dagger_V\hat{b}^\dagger_V\right)|0\rangle_{ab} = \\ &= \left(\hat{a}^\dagger_V\hat{a}^\dagger_V - \hat{b}^\dagger_V\hat{b}^\dagger_V\right)|0\rangle_{ab} = \\ &= \frac{1}{\sqrt{2}}\left(|2;V\rangle_a - |2;V\rangle_b\right)\end{aligned} \tag{1.48}$$

In this case the states related to one photon for each output port of the beam splitter vanish. This means that the probability of having a coincidence is equal to zero. When we have perfectly indistinguishable photons they always exit coupled after interacting with a beamsplitter.

The crucial part of this analysis is that in order to see the HOM interference the two photons must have identical physical properties, such as polarization, spatio-temporal mode structure, and frequency.

In this case the photons are assumed to interact at the same time with the beamsplitter. In an experimental setup, however, a time delay can be added to tune their level of indistinguishability.

Moreover, they are generated in the same state. This means that they have the same spectral properties. The wavepacket associated to both the photons is exactly the same, i.e. they have a constant phase relation during the time duration of the wavepacket. This means that an important parameter in order to obtain a good HOM interference between photons is the coherence length of the photons we are considering. If they have a low coherence degree the photons are partially distinguishable, and the HOM interference dip is reduced, or vanishes. The result from the original article about HOM interference is shown in figure 1.18. Here $\tau$ is the time delay between the photons. As can be seen, if the time delay is equal to 0 the coincidence counts drop to 0. The shape and the width of the dip depend on the the spectral function of the photons [48].

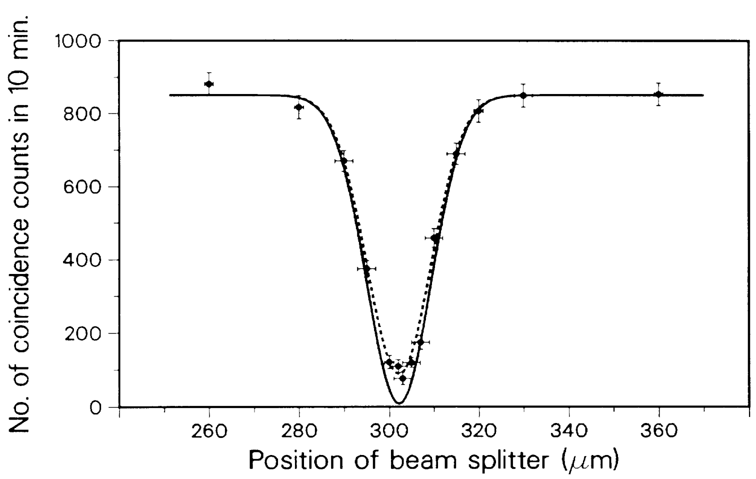

Figure 1.18: Graphic of the HOM interference from the original article published by Hong-Ou-Mandel [47]. Here the number of coincidence counts measured in ten minutes is plotted versus the displacement of the beam splitter. When its position is such that the two photons arrive interacts at the same time with it, the number of counts diminishes.

# Chapter 2

# Development of the experimental Setup

## 2.1 Cooling system

In order to make measurements with quantum dots it is necessary to cool them down to low temperatures, hence reducing the system energy. This causes a reduction of transitions between energy levels associated to thermal energy and a reduction of background noise. Once cooled, the sample can be excited with a laser, and its emission spectrum can be characterized.
The electron occupation probability of a state with energy $E$ inside a semiconductor follows the Fermi-Dirac distribution, which is plotted in figure 2.2 for different values of the ratio $E/E_F$

$$f(E,T) = \frac{1}{e^{\frac{E-E_F}{kT}} + 1} \tag{2.1}$$

where $k$ is the Boltzmann constant, $T$ the absolute temperature and $E_F$ the Fermi energy of the system, i.e. the highest kinetic energy of the occupied states.

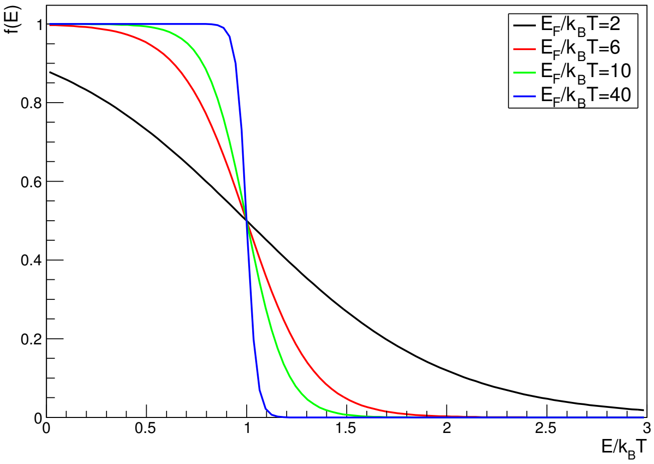

Figure 2.1: Plot of the Fermi distribution for different values of the ratio $E_F/k_BT$.

The Fermi energy is usually in the middle of the bandgap for intrinsic semiconductors, with a linear dependence on the temperature [49]

$$E_F = \frac{E_V + E_C}{2} + \frac{k_B T}{2} \ln\left(\frac{N_v}{N_c}\right) \tag{2.2}$$

where $E_V$ and $E_C$ are the energies of the valence and conduction band, and $N_v$ and $N_c$ are the effective density of states in the valence and conduction band. With an extrinsic semiconductor, the Fermi energy moves closer to the conduction band if the material is n-doped, while it moves closer to the valence band if the material is p-doped.

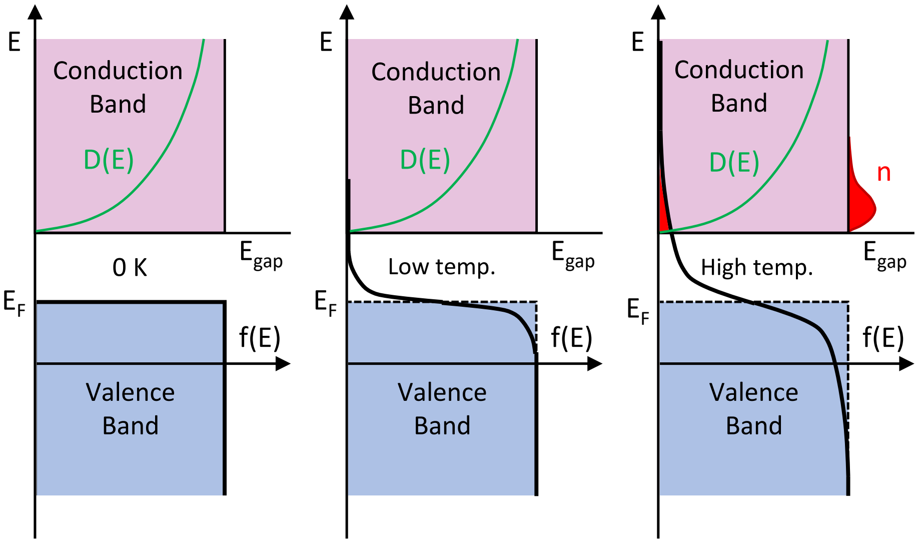

Figure 2.2: Schematics showing the density of electrons in the conduction band at different temperatures in a bulk semiconductor. As we can see, for high temperatures the Fermi distribution becomes $f(E)$ becomes broader and there is a non-null probability of having electrons in the conduction band. This leads to a high density of electrons in the conduction band $n$, which is calculated as written in equation 2.3.

In order to calculate the density of electrons inside the conduction band the density of states as function of the energy must also taken into account. Usually the electron density is calculated as

$$n = \int_{E_C}^{\infty} D(E) f(E,T) dE \tag{2.3}$$

As known from section 1.2 a bulk material has a density of energy states $D(E) \propto \sqrt{E}$. Making the calculations, the density of electrons in the conduction band is equal to [50]

$$n = 2\left(\frac{m_n^* k_B T}{2\pi\hbar^2}\right)^2 e^{-\frac{E_C - E_F}{k_B T}} \tag{2.4}$$

where $m_n^*$ is the effective mass of the electrons.
If a commonly used semiconductor for quantum dots like InAs is considered, which has a bandgap energy equal to 0.415 eV at 4.2 K [51], The Fermi energy will be about 0.207 eV for low temperatures. Using the formula 2.4 the electron density in the conduction band

equal can be approximated to 0, while at room temperature we usually have $n \sim 10^{22}$. Therefore reducing the temperature to 4.2 K makes very unlikely the chances of having an electron in conduction band due to a thermal transition. This means that the background noise due to this source is strongly reduced.
Considering that due to its three dimensional spacial confinement a quantum dot has discrete energy states 1.2, this transition probability becomes even lower.
Reducing the noise given by thermal excitation is then the reason why the system is cooled down to 4.2 K. Once cooled down the sample to this temperature it is possible to excite the quantum dot and treat it like a two-level system. The cryostat model is a *Montana Instruments cryostation s50.*

Inside the cryostat the position of the sample is piezo controlled. In this way we are sure that we are hitting exactly the quantum dot with the laser.

## 2.2 Imaging of the sample

The sample can be observed trough a microscope system containing two lenses. The first one is placed above the access window of the vacuum chamber. With a differential micrometer screw we can adjust the position of this lens in the vertical direction over the cryostat to achieve the correct focus. The reflected beam is then sent to another lens, and it is collected by a CCD camera. The sample is illuminated using a diode. The light it emits is collected through a lens, which collimates the beam, and then focused on the sample with the same method described above. Since to access the window of the cryostat the beam has to come from above, a periscope was built to lift the beam and direct it from above to the sample. In figure 2.3 a schematic of this part of the setup is shown, while an image of the sample taken with this method can be seen in figure 2.4. These are nanowires embedding a single quantum dot each. For the excitation it was used a 635 nm continuous wave laser and a Ti:Sapphire pulsed laser that will be described in the section 2.4. The excitation scheme we use is called collinear because the incoming beam and the photons emitted by the QD follow the same path.

## 2.3 Spectroscopy methods

In our experimental setup we used two different kinds of spectrometers: a commercial one from Princeton Instruments, used to get a general overview of the spectra we are taking, and a self-made spectrometer, used to discriminate between the exciton and the biexciton lines of our QDs' spectra.

### 2.3.1 Princeton Instruments spectrometer

The Princeton Instruments spectrometer is connected to a CCD camera, which has a quantum efficiency above 80 % between 400 and 900 nm. Since these cameras are sensitive to single photons, it is necessary to reduce the dark current and the thermal noise typical of these devices. This is the reason why the camera has a thermoelectric cooling to $-70^{\circ}$ [52]. In this way we are able to observe also the photons emitted by a single

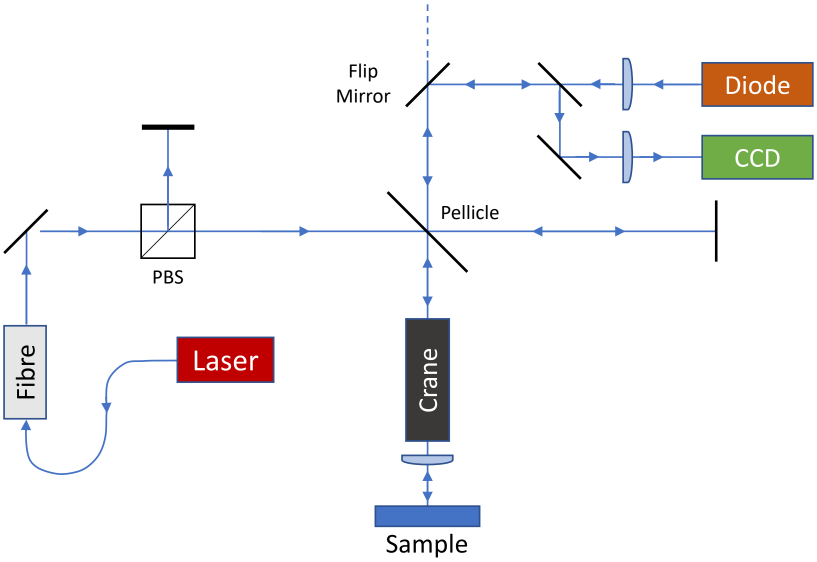

Figure 2.3: Sketch of the optical line built for the imaging and excitation system. For the imaging system The light from the diode is collimated and focused on the sample. Then the reflection is sent back on the same path and focused on the CCD. The mirror on the right side of the pellicle beamsplitter (polarization beamsplitter with asymmetric splitting ratio) was used for the allignment of the beam.

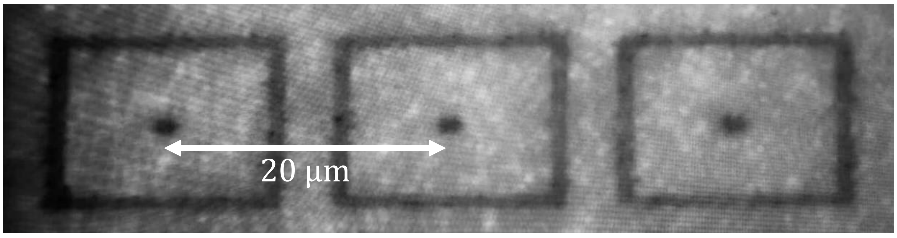

Figure 2.4: Image of the sample obtained with the imaging system described above. These are nanowires embedding quantum dots.

quantum dot. Moreover, since the camera is very sensitive, the spectrometer has two shutters, one for each input port, that prevents the chip from being damaged by the incoming light. This shutter can also be set as always open, always closed and normal, which means that it opens and closes every time just for the exposure time that is set.
The spectrometer's configuration is illustrated in Figure 2.5: it has two different input ports, with two slits, one for each port, which reduce the background light. The focal point of the beam must be on the slits, and the beam must be well aligned when it passes through the slits. The beam is reflected by a concave mirror, which collimates it into a blazed diffraction grating. This grating diffracts the light and sends it to another concave mirror, that focuses the beam onto the camera.
The output signal from the camera can be analyzed with a software developed by Princeton instruments. With this software also several useful parameters can be set. For example, the area of the chip used for taking data can be selected, the *Region of Interest*

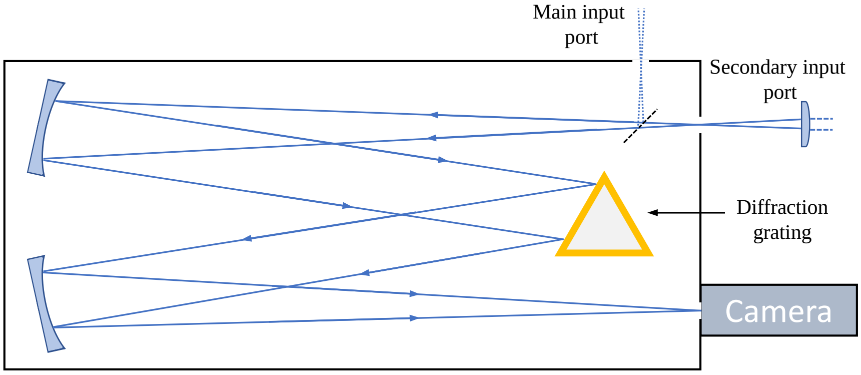

Figure 2.5: Sketch of the Princeton Instruments used in the setup. The beam is focused on the input slit, collimated by a spherical concave mirror and then diffracted by a blazed diffraction grating. At the end it's reflected by another concave mirror and focused on a CCD camera, cooled at $-70°$ C. when we cool the camera we reduce the dark counts due to the thermal energy, and this makes us able to observe even single photons emitted by our quantum dot.

(RoI). In this way only the data around the spot we are interested in can be selected (Figure 2.6). The output from the software is a matrix of numbers (one for each pixel) proportional to the intensity of the light that is hitting the CCD. During the data acquisition the output from each pixel in a column is summed, obtaining a single value of the intensity for each wavelength. If only a small portion around the light spot is considered, summing the bins allows to reduce the background noise, compared to the case where we consider all the chip of the camera.
Both the input ports are used, with the main input port used to see the emission spectra of the quantum dots we excite, and the secondary port used to see other spectra, like the one from the Ti:Sapphire laser or from the pulse stretcher.

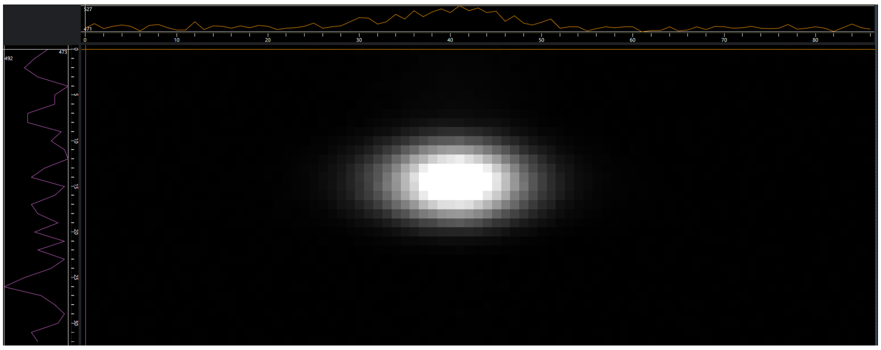

Figure 2.6: Screenshot from the Princeton spectrometer software. This is the considered region of interest. The spot corresponds to the beam sent in the spectrometer and that is diffracted by the grating. The output of this software is a matrix of numbers, one for each bin inside the RoI. In our case we sum over all the bins of each column. In this way we obtain a better defined peak and reduce the background (compared to the peak).

This spectrometer is useful because enables to have a fast overview of the spectrum of the quantum dot we are exciting, and it was used to characterize their emission, for example under above band excitation (section 3.1. Unfortunately with this spectrometer it is impossible to separate the path of the photons belonging to these excitation lines, and this problem makes it unsuitable for other kind of measurements, like the cross-correlation between the photons from the exciton and the biexciton. This is the reason why also a self-made spectrometer was built.

### 2.3.2 Self-made spectrometer

With the self-made spectrometer we can measure the signals from the biexciton and exciton photons at the same time. It consists essentially in a blazed diffraction grating. The grating is mounted on a computer-controlled rotation stage. The incident light is reflected and diffracted in multiple directions, depending on the wavelength. A schematics of diffraction gratings can be seen in Figure 2.7. The path difference between two rays is equal to $d \sin \alpha + d \sin \beta$ (where $\beta$ is a negative angle, and $d$ the distance between two grooves). in order to obtain a constructive interference between these two rays this optical path difference must be a multiple of the wavelength. We obtain then the *grating equation* [53]:

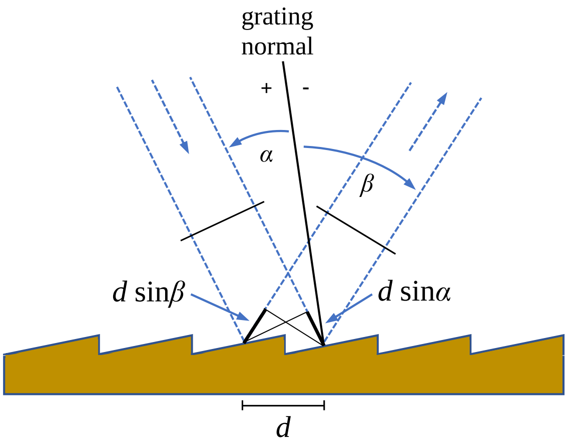

Figure 2.7: Scheme of a blazed diffraction grating. The black solid line is the normal to the grating.

$$m\lambda = d(\sin \alpha + \sin \beta) \tag{2.5}$$

where $m$ is the diffraction order and $\lambda$ the wavelength of the incoming beam. This equation tells us at which angle the outcoming beam is diffracted. As we can see, if $m = 0$ we obtain a simple reflection, with $\alpha = -\beta$.

Blazed diffraction gratings are made in such way that they maximize the amount of light in one specific order for one wavelength. The diffracted beam has its highest intensity when it comes back in the same direction as the incident beam, this is the so called *Littrow configuration*. Using this equation we calculated then the angle $\beta$ at which the beam is diffracted. Since we have fixed input and output angles, we have to rotate the grating in order to obtain the maximum diffracted intensity at the output angle for the wavelength we are using.

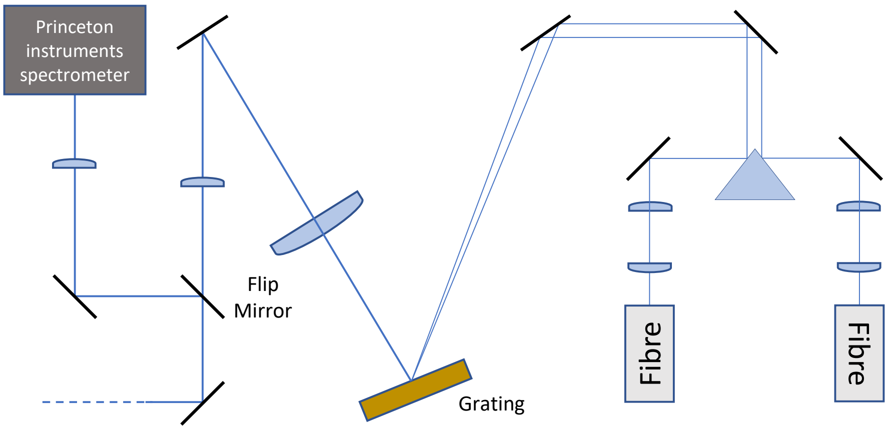

Figure 2.8: Design of the self-made spectrometer. The beam is magnified and collimated with a telescope, and is diffracted by the diffraction grating. The beam is then sent through a lens and focused on a knife edge prism, where we separate the exciton and the biexciton photon. Afterwards the two beams are coupled in two fibers, connected to APDs.

The configuration of the self made spectrometer can be seen in Figure 2.8 : The beam is magnified and sent on the diffraction grating, we want in fact to maximize its resolution. Resolution or ”chromatic resolving power” for a device used to separate the wavelengths of light is defined as [54]

$$R = \frac{\lambda}{\Delta\lambda} \tag{2.6}$$

where $\Delta\lambda$ is the smallest resolvable wavelength difference. The resolving power gives an expression of if two spectral lines can be seen as two different lines.
The limit of resolution is determined by the Rayleigh criterion as applied to the diffraction maxima, i.e., two wavelengths are just resolved when the maximum of one lies at the first minimum of the other. This means that equality between the maximum at wavelength $\lambda + \Delta\lambda$ and the minimum at $\lambda$ is satisfied :

$$Nd\sin\theta = Nm(\lambda + \Delta\lambda) \qquad = \qquad Nd\sin\theta = Nm\lambda + \lambda \tag{2.7}$$

where $d$ corresponds to the distance between two slits, $N$ is the number of slits illuminated and $m$ is the order of diffraction. This gives us

$$R = mN \tag{2.8}$$

This equality depends on the diffraction order of interest and is proportional to the number of groves that are illuminated, and means that the higher is our resolution, the bigger is the separation between different wavelengths.
Taken two lines separated by $\Delta\lambda$ and with central wavelength $\lambda$, they are resolved if

$$R = mN > \frac{\lambda}{\Delta\lambda} \tag{2.9}$$

The beam is diffracted by the grating, and focused on a knife edge prism. With this prism we separate the two beams, which are coupled into two single-mode fibres.
After the coupling, the fibers are connected to two *Avalanche PhotoDiodes* (APDs). The signal from the APDs is then sent into a Time to Digital Converter (TDC), which is connected to the computer. A TDC is a device that is commonly used to measure a time interval and convert it into a digital signal. In it's simplest configuration, a TDC is a high-frequency counter which increments its counts every clock cycle. For higher resolutions, a higher frequency is needed. Our TDC has a time resolution of 1 ps [55]. Often it's more useful to measure time intervals. When used for this purpose, two different signals are sent into the device, one starts the counter and the other one stops it. This device has many application in physics, and in our case it's useful when we want to measure the autocorrelation and the cross-correlation between the photons emitted by the quantum dot.
Using a graphical user interface it is possible to control the rotation grating of the self-made spectrometer stage and see the number of counts. With this program is also easy to see the coincidence counts, and the correlation and auto-correlation plots between the photons emitted by the QD.

## 2.4 Optical line characterization

In order to design an optic line is crucial characterizing the propagation of the beam. The light from a laser is emitted with particular spatial and frequency distributions, depending on the boundary conditions for resonance on the cavity, called modes. A transverse mode is a particular pattern of the electromagnetic field measured in a plane perpendicular to propagation direction. The modes are denoted with TEM$_{pl}$ (transverse electromagnetic), where $p, l$ are the radial and angular modes. The output of the used Ti:Sapphire laser is the fundamental mode TEM$_{00}$. With this mode the intensity profile has a gaussian shape, that for a beam propagating along the $z$ axis is equal to

$$I(r) = I_0 \left[\frac{w_0}{w(z)}\right]^2 e^{-\frac{2r^2}{w(z)^2}} \tag{2.10}$$

where $w(z)$ is the distance from the beam axis where the intensity is equal to $1/e^2$ times the maximum value, and $r$ is equal to $\sqrt{x^2+y^2}$. Because of its shape, this beam is called gaussian beam. This beam is one of the solutions of the wave equation. This solution is obtained starting from the parabolic solution. Here a monochromatic spherical wave with origin in $\mathbf{r} = 0$ is considered (with complex amplitude equal to $U(r) = \frac{A}{r}e^{-ikr}$). The wave is considered far from its origin, and close to a $z$ axis, such that $\sqrt{x^2+y^2} \ll z$. In this way the radius $r$ can be written as

$$r \sim z + \frac{x^2+y^2}{2z} \tag{2.11}$$

and the corresponding complex amplitude can be written as

$$U(r) = \frac{A}{z}e^{-ikz}e^{-ik\frac{x^2+y^2}{2z}} \tag{2.12}$$

Close to the z axis this wave can be approximated as a plane wave. If the normals to the wavefronts form a small angle with the propagation direction the waves are called *paraxial waves*. In this case the complex amplitude is taken as

$$U(r) = A(r)e^{-ikz} \tag{2.13}$$

The gaussian beam is obtained substituting $z$ with a complex parameter $q(z)$. $A(\mathbf{r})$ becomes

$$A(\mathbf{r}) = \frac{A_1}{q(z)}e^{-ik\frac{\rho}{2q(z)}} \tag{2.14}$$

where $q(z) = z + iz_0$ and $\rho^2 = x^2 + y^2$. $z_0$ is called *Rayleigh range*. With this complex parameter the intensity, calculated as $I(\mathbf{r}) = |U(\mathbf{r})|$ has the gaussian profile written in equation 2.10. With this solution she beam waist and the radius of curvature of the wavefront evolve in space in the following way:

$$w(z) = w_0\sqrt{1 + \left(\frac{z}{z_0}\right)^2} \qquad R(z) = z\left(1 + \left(\frac{z_0}{z}\right)^2\right) \tag{2.15}$$

where $w_0$ is the minimum waist of the beam, i.e. the waist at the focal point. From the first equation is easy to understand that the Rayleigh range is the distance from the focus where the beam waist is equal to $\sqrt{2}$ times the minimum waist. The Rayleigh range can be written as function of $w_0$, as $z_0 = \frac{\pi w_0^2}{\lambda}$. All the beam is determined by the parameter q(z).

The propagation of a gaussian beam is shown in figure 2.9. The curvature radius of the wavefront is negative before the focus, and positive after it. When $|z| \gg z_0$ $w(z)$ the beam expands linearly in space and $w(z)$ can be approximated as

$$w(z) \simeq \frac{\lambda}{\pi w_0}z = \theta_0 z \tag{2.16}$$

The angle $\theta_0$ is called *divergence angle*. As can be seen, the divergence angle is proportional to the wavelength and has an inverse relationship to the beam waist. This means that an highly focalized beam has a large divergence, and in order to obtain a collimated beam is useful to use a long wavelength and a large waist.

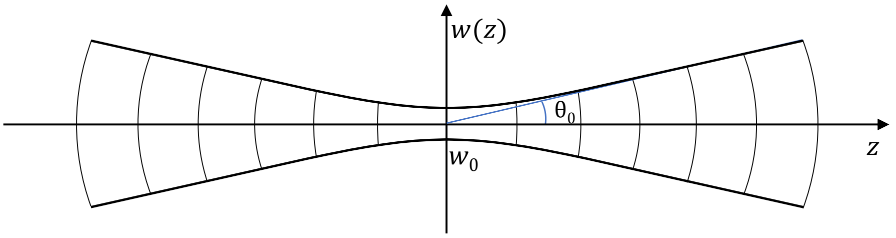

Figure 2.9: Propagation of a gaussian beam along an axis z. $w_0$ is the minimum wais of the beam. The radius of curvature of the wavefront change sign after $w_0$, and is infinite in $w_0$.

In order to characterize the beam some measurements of the waist were taken with the razor blade method. Here the beam is cut with a sharp blade, and the remaining power of the beam is measured with a power meter (Figure 2.10). Since the intensity has a gaussian profile, the measured power will be

$$P(x) = \int_{-\infty}^{x} \int_{-\infty}^{+\infty} I(x,y)\,dx\,dy = A\,\mathrm{erfc}\left(\frac{x - x_c}{\sqrt{2}w(z)}\right) \tag{2.17}$$

where $A$ is a constant, $x_c$ is the center of the beam and $w(z)$ is the waist at the measured point. An example of this measurement can be seen in figure 2.10. The waist was measured as

$$w = \frac{x_{86.5} - x_{13.5}}{2} \tag{2.18}$$

where $x_{86.5}$ and $x_{13.5}$ are respectively the points where the intensity is $1 - 1/e^2$ and $1/e^2$ times the maximum intensity.

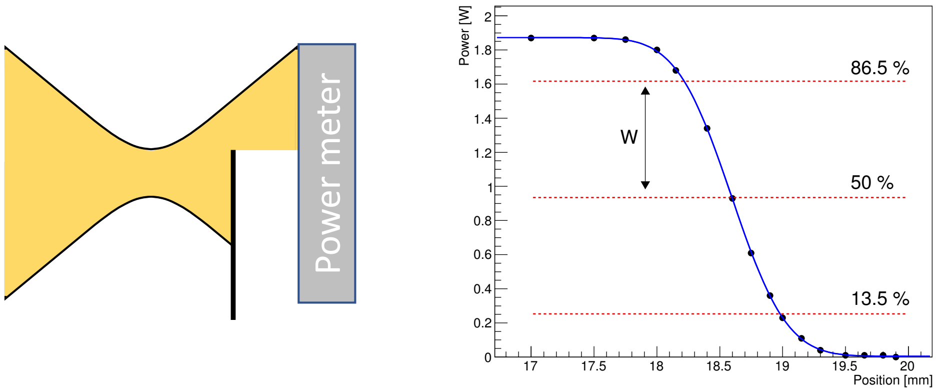

Figure 2.10: Left: schematics of the razor blade method for measuring the waist The beam is cut with a sharp blade and the remaining power is measured with a power meter. Right: example of the measurement of the waist with this method. The error function can be seen. The waist is measured as $w = (x_{86.5} - x_{13.5})/2$.

After measuring some points with this method, the q-parameter was calculated and the propagation of the beam modeled, using the first of equations 2.15. With a real gaussian beam these equations must be modified taking into account the $M^2$ parameter. It is defined from the relation

$$w_0\theta_0 = \frac{M^2\lambda}{\pi} > \frac{\lambda}{\pi} \tag{2.19}$$

where $w_0$ is the minimum waist of the beam, and $\theta$ is the divergence angle of the beam. In this case, since it was close to the unity, $M^2$ was approximated to 1. Afterwards using the matricial optic formalism [56] the propagation of the beam through two lenses was modeled. With the optical matrices formalism (also called the *ABCD formalism*) each element of the optical line is modeled using a 2x2 matrix, and the effect of all the optical system on the beam is the product of these matrices, from the last optical element to the first one.

$$\mathbf{M}_i = \begin{pmatrix} \mathrm{A} & \mathrm{B} \\ \mathrm{C} & \mathrm{D} \end{pmatrix} \qquad \mathbf{M} = \mathbf{M}_n \cdot \mathbf{M}_{n-1} \ldots \mathbf{M}_2 \cdot \mathbf{M}_1 \tag{2.20}$$

The q parameter after all the system is then calculated as

$$q(z) = \frac{\mathrm{A}q_0 + \mathrm{B}}{\mathrm{C}q_0 + \mathrm{D}} \tag{2.21}$$

where $q_0$ is the initial q parameter.

## 2.5 Pulse stretcher

As previously described (Section 1.2), due to their three dimensional spatial confinement quantum dots have discrete energy levels, and then spectra with discrete emission lines. These lines show a broadness due to different reasons.
Our goal is exciting the QD through a resonant excitation. If we want to use a resonant excitation or the two-photon resonant excitation (section 1.3), in both cases we need to reduce as much as we can the spectral width of our laser. In case of a two-photon resonant excitation we want to lower the effect of laser scattering and reduce the overlap between the laser and the exciton - biexciton lines. A Ti:Sapphire laser is used in order to excite resonantly the quantum dot. It is a pulsed laser with 140 fs pulse duration (taken as FWHM), and a pulse repetition rate of 80 MHz. This laser has a tunable wavelength from 720 to 980 nm. The output power is equal to 0.6 W at 720, then goes up to 1.7 W at 800 nm and decreases to 0.45 W at 980 nm. Since it emits ultra-short pulses, its emission spectrum is broad. The laser spectrum can be made narrower building a pulse stretcher: this tool is based on the concept that the Fourier transform of a narrow distribution in the time space corresponds to a broad distribution in frequency space. Therefore, if a Fourier transform of our beam can be made and some frequencies can be cut, then after the inverse Fourier transform the laser pulse will have a longer duration in time space. Let's see not only qualitatively the relation between the time duration of a light pulse and its spectral width.
A monochromatic plane wave is defined with the following time dependence:

$$E = \Re(E_0 e^{i\omega_0 t}) \tag{2.22}$$

This is an unlimited cosine function. If a pulse must be considered (i.e. a Gaussian pulse) the function will be [57]

$$E = \Re(E_0 e^{-\Gamma t^2 + i\omega_0 t}) \tag{2.23}$$

where $\Gamma \propto t_0^{-2}$, and $t_0$ is the time duration of the pulse.
The spectral width of the pulse is then calculated as the modulus of the Fourier transform of the function 2.23. The Fourier transform of a gaussian function is another gaussian function, whose width is related to the time duration of the pulse. The time and frequency Fourier transform of a pulse can be written as

$$\varepsilon(t) = \frac{1}{2\pi}\int_{-\infty}^{+\infty} E(\omega)e^{-i\omega t}\mathrm{d}\omega \qquad E(\omega) = \int_{-\infty}^{+\infty} \varepsilon(t)e^{i\omega t}\mathrm{d}t \tag{2.24}$$

The duration and spectral width of the pulse are calculated in the following way:

$$\langle \Delta t \rangle = \frac{\int_{-\infty}^{+\infty} t|\varepsilon(t)|^2 \mathrm{d}t}{\int_{-\infty}^{+\infty} |\varepsilon(t)|^2 \mathrm{d}t} \tag{2.25}$$

$$\langle \Delta \omega^2 \rangle = \frac{\int_{-\infty}^{+\infty} \omega^2 |E(\omega)|^2 \mathrm{d}\omega}{\int_{-\infty}^{+\infty} |E(\omega)|^2 \mathrm{d}\omega} \tag{2.26}$$

It can be demonstrated that the relation between these two quantities is

$$\Delta t \Delta \omega \geq \frac{1}{2} \tag{2.27}$$

and the equality is satisfied when the two pulses are Gaussian-shaped.
From an experimental point of view is easier to measure the FWHM of a pulse, so the equation 2.27 is usually written as $\Delta\nu\Delta t = K$, where K is a constant which depends on the shape of the pulse. For a Gaussian pulse, $K = 0.44$ [57].

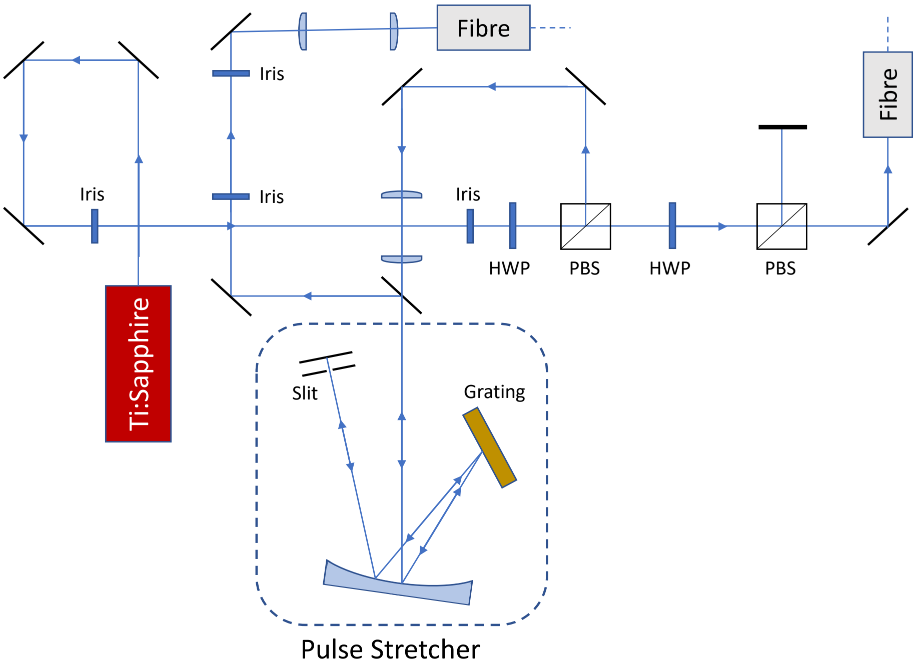

Figure 2.11: Design of the optical line. On the lower part the pulse stretcher can be seen. Here the beam is diffracted on a blazed diffraction grating and is focused on a slit. Then, reflected by a flat mirror, goes back a bit displaced and it's extracted using a prism. In this way we can separate the beam we obtain from the one coming from the fibre, and at the end we couple it in another fibre.

Essentially the setup of the pulse stretcher consists of a diffraction grating and a slit. The beam derived from the laser was sent to the grating, in order to make the Fourier transform of our beam. Since diffraction angle depends on wavelength we are separating

different wavelengths and switching to frequency domain. After that the frequencies are cut by the slit.
In order to obtain a larger spatial separation between the wavelengths the resolution of the grating (as written in section 2.3) has to be maximized. This is the reason why a telescope is built before the stretcher.

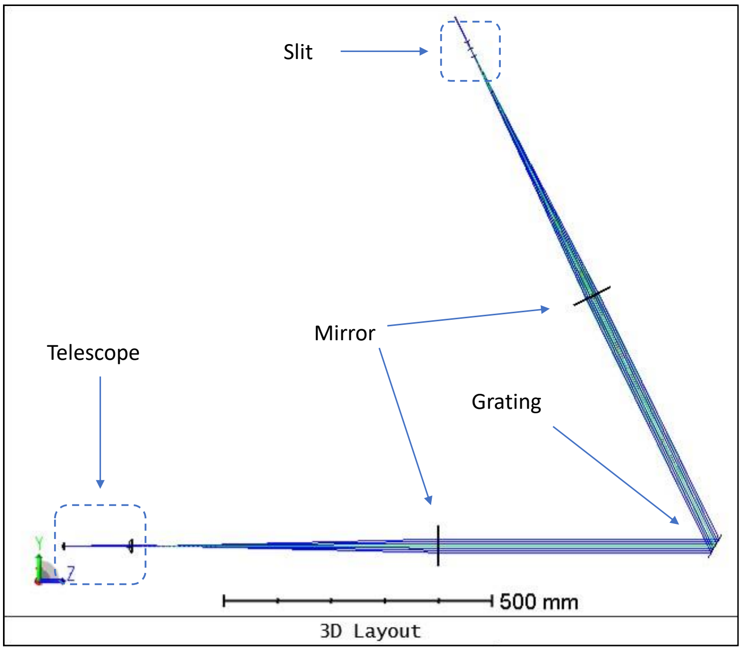

Figure 2.12: Picture from Zemax Optic Studio, describing the design of the pulse stretcher. The telescope was made using two convex lenses. We used a concave mirror, with a long focal length, that was placed in such a way that we obtained a collimated beam after the telescope. The beam was focused then on a slit.

The pulse stretcher was built using compact 4-f configuration [58], as shown in the lower part of figure 2.11. With this configuration the beam is first collimated by the concave mirror and diffracted by the grating. Then the beam is reflected again in the mirror and focused on a slit, which cut the external frequencies of the laser spectrum. Behind the slit is placed a flat mirror, which reflects the beam along almost the same path. This out-coming beam is extracted using a prism, then it is coupled in a fibre, using another telescope.

This stretcher was designed using Zemax Optic Studio. Two convex lenses are used for the telescope. Then it is used a big concave mirror with long focal length. The long focal length of the mirror is chosen to obtain a larger spatial displacement between the different wavelengths along the propagation. This fact can be useful in order to obtain a narrower spectrum when the beam is cut by the slit. The mirror is placed at the focal length from the focus of the beam, so that it collimates our beam, which goes on a blazed diffraction grating. In the end the beam passes through a square slit. A flat mirror is placed 1 cm behind the slit. The stretcher can be seen in figure 2.12. The central wavelength was set equal to 880 nm. This wavelength was chosen because is close to the transition

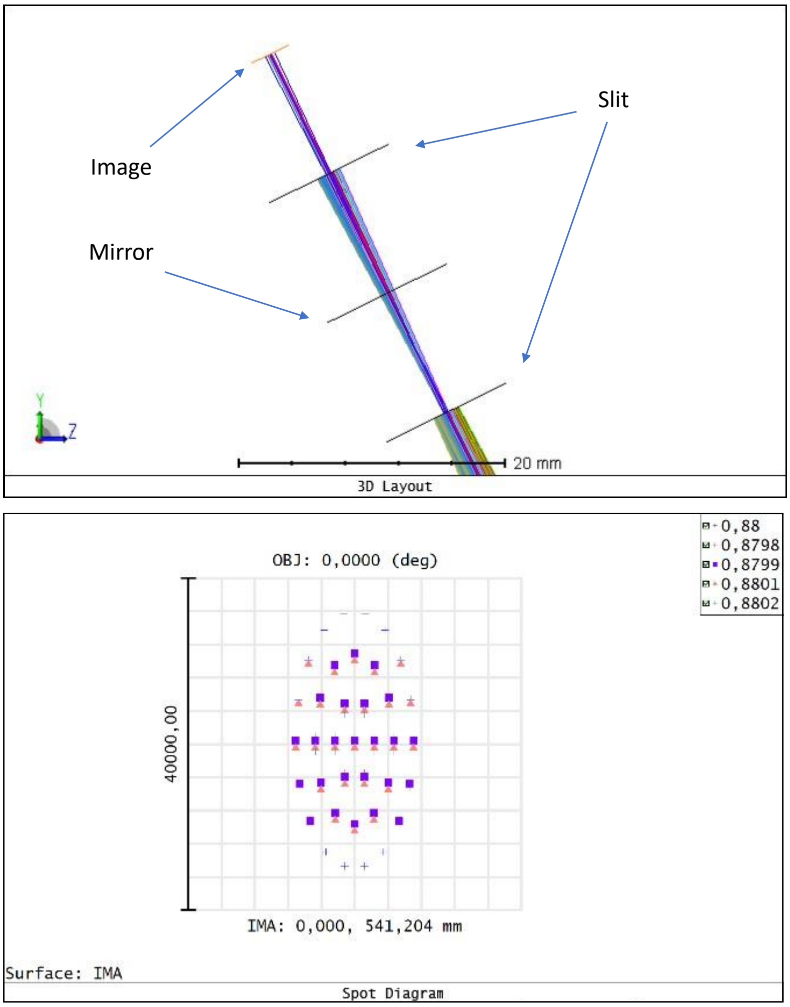

Figure 2.13: Pictures taken from Zemax Optic Studio. Top: part of the design with the slit and the mirror. Since the crucial part of the stretcher is which interval of wavelengths goes through the slit, we stopped after passing through the slit two times. Bottom: the corresponding spot diagram (taken on the orange surface). We obtain a 0.4 nm interval width, with 880 nm as central wavelength (we started from an interval width of 1 nm). This FWHM spectral width corresponds (using this wavelength) to a pulse duration of 2.65 ps. Considering that we started from 140 ns, the duration pulse was increased 20.4 times.

wavelengths of most the InAs/GaAs quantum dots. Moreover the spectral width depends not only on the time duration of the pulse, but also on its central wavelength.

Since Zemax Optic Studio was used in sequential mode, where the beam can pass through a surface only once, for simplicity after the diffraction the beam goes on another concave mirror. Moreover, even if we are using mirrors, the beam propagates through them (and the flat mirror is modelled just as an empty surface). Since the crucial part of the stretcher is which interval of wavelengths goes through the slit, the propagation of the beam was stopped after passing through the slit two times (Figure 2.13, top). After

passing through the slit two times the wavelengths that are still in the beam are observed through the tool *Spot Diagram* (figure 2.13, bottom). This tool enables to project on a surface the beam of our optical system, and look at its shape or, in our case, the spatial distribution of its wavelengths. We decided to use this tool at the orange surface that can be seen on the top of Figure 2.13.
For a 140 fs long pulse at that wavelength the spectral FWHM is 8.14 nm. Looking at the *Spot Diagram* it can be seen that this configuration of the stretcher accepts a wavelengths interval equal to 0.4 nm. This means that, making the inverse Fourier transform, a 2.85 ps pulse is obtained, increasing of a factor 20.4 its temporal width. In this design the light spectrum is assumed to be a square function, but actually it's a Gaussian-shaped function, so when a narrower FWHM is expected when the experimental width of the spectrum will be measured.

After assembling the stretcher the output fiber was connected to the secondary input port of the spectrometer. The original spectrum of our Ti:Sapphire was first observed using the out-coming beam from the second beam splitter. This spectrum can be seen in Figure 2.14. Making a Gaussian fit of our spectrum a FWHM equal to 8.24 nm is obtained, which is in good agreement with the prediction we made. the second peak is probably due to the fact that inside the cavity there are other frequencies allowed, corresponding to wavelengths about 855 nm.

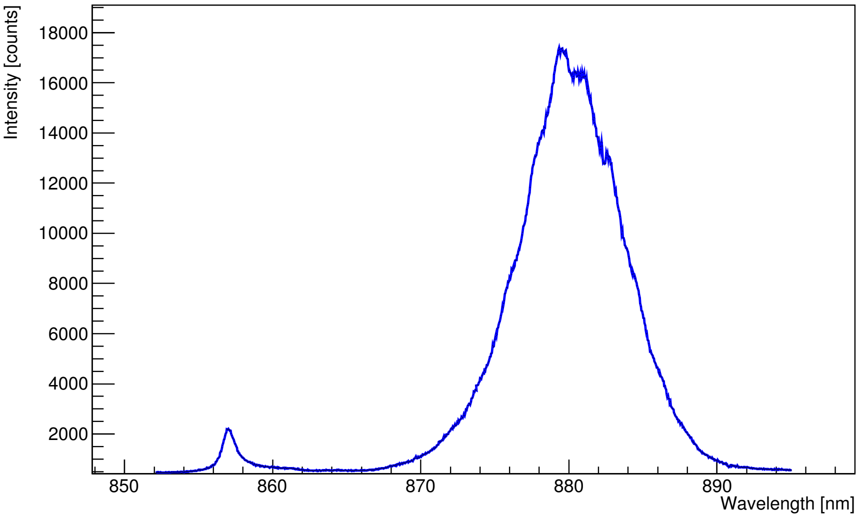

Figure 2.14: Spectrum of the Ti:Sapphire laser acquired with the 600 gr/mm grating. Doing a Gaussian fit on our main peak we obtain a FWHM equal to 8.24 nm, measurement that is in good agreement with the prediction we made.

Finally the output of the pulse stretcher was observed, and plotted for different widths of the slit in the Figure 2.15. Since the diffracted beam is bigger than the slit, it is impossible to see all the spectrum after the stretcher.
The output of the stretcher was optimized moving the slit along the propagation of the beam, and verifying the shape and the FWHM of the resulting spectrum. For positions far from the focal point of the beam the spectrum in fact shows a strong asymmetry, with

two different slopes at the two sides of the peak (one sharper than the other). Depending on where the slit is placed (before or after the focus), these different slopes invert the sides. When there is a symmetric shape it means that the slit is placed closer to the focal point of the beam (Figure 2.16). Moreover to the symmetric shape of the peak corresponds the smallest FWHM.

Closing the slit the minimum FWHM obtained is equal to 0.215 nm. This width corresponds to a 5.4 ps long pulse for the used wavelength (880 nm). In this way almost 3.7 % of the spectrum is selected, and the output power is equal to 3 % of the incoming power. This means that about 20% of the power is lost going through the stretcher.

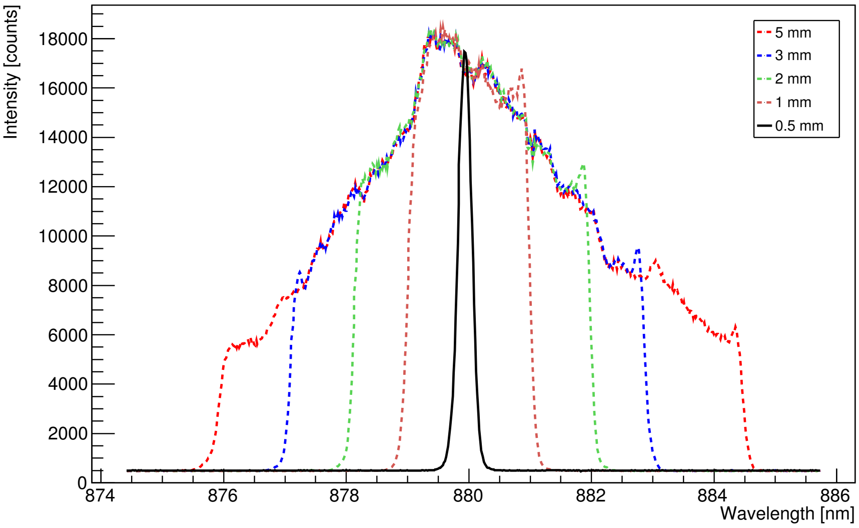

Figure 2.15: Spectrum of our laser after the pulse stretcher, acquired using the 1200 gr/mm grating. Closing the slit and doing a Gaussian fit on the peak a FWHM equal to 0.215 nm is observed. This spectral width corresponds to a 5.4 ps long pulse.

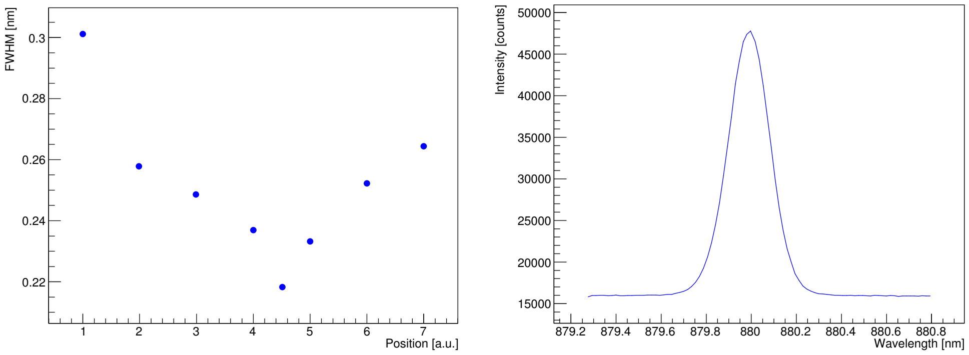

Figure 2.16: Left: FWHM of the spectrum obtained from the stretcher at different positions of the slit. Right: Spectrum with the minimum FWHM.

## 2.6 Interferometer

An important property of the quantum dot's emitted photons is their coherence length. The coherence length is the propagation distance over which the wave maintain a stable phase relation. As pointed out in section 1.5, in order to obtain a good HOM interference two photons must be exactly in the same state, i.e. they must have the same spectral and temporal properties, and the same polarization. This means that their wavepackets must be the same, and have a constant phase relation during their temporal length.
Measuring the coherence length hence gives an estimation of the "quality" of the emitted photons, and then of the used quantum dot. Sources of dephasing are usually the interactions between our quantum dot and the environment. These interactions cause fluctuations of the QD energy levels (called *jittering*) that seriously decrease the coherence length of the emitted photons. Moreover, as said in section 1.3, other dephasing sources are the relaxation processes through phonon scattering and Coulomb interactions between carriers [59] [60], when the quantum dot is non-resonantly excited.

Wave interference is strong when the paths taken by all of the interfering waves differ by less than the coherence length. Therefore measuring interference is a good way to measure the photons' coherence length. For this reason a Michaelson interferometer was built, with the setup that can be seen in figure 2.17.

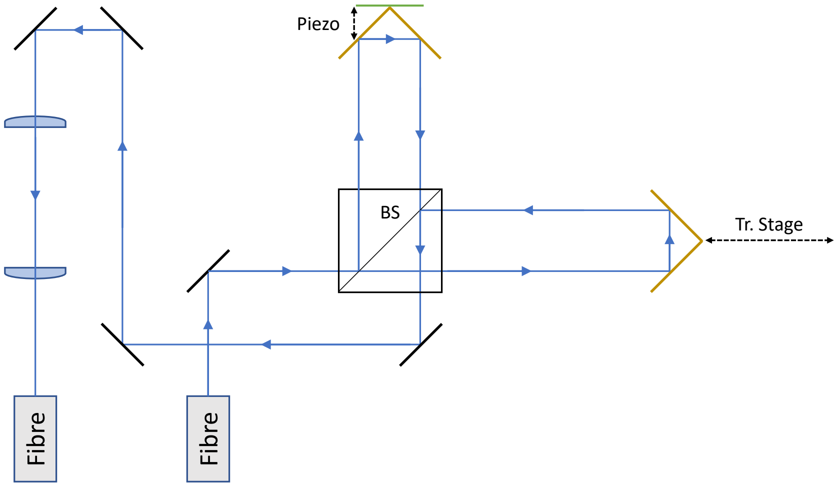

Figure 2.17: Design of the Michaelson interferometer. The beam is sent to a 50:50 beam splitter and then to two retroreflectors. The beams go back to the beamsplitter, where they interfere. The resulting beam is then coupled through two lenses into an high power polarization maintaining single mode fiber.

Let's assume that the input radiation has a constant amplitude equal to $E_0$, and a fixed wavelength equal to $\lambda$. The output electromagnetic field will be

$$E_{out} = E_1 + E_2 \tag{2.28}$$

where $E_1$ and $E_2$ are the fields coming from the two arms of the interferometer, with lengths equal to $L_1$ and $L_2$. Using the complex notation, $E_{out}$ can be written in the following way:

$$E_{out} = \frac{E_0}{2} e^{ik2L_1} + \frac{E_0}{2} e^{ik2L_2} e^{i\delta_{\text{ref}}} \tag{2.29}$$

where $E_0/2$ is given by the fact that the photons go through a 50:50 beamsplitter, $k$ is the wave number, equal to $2\pi/\lambda$, and the term $\delta_{\text{ref}}$ is a phase term due to the reflection at the beamsplitter of one of the two beams. This formula can be also written as

$$E_{out} = \frac{E_0}{2} e^{ik2L_1}(1 + e^{i\delta}) \tag{2.30}$$

where was used $\delta$

$$\delta = k2\Delta L + \delta_{\text{ref}} \qquad \Delta L = L_2 - L_1 \tag{2.31}$$

The value of $\delta_{\text{ref}}$ will be equal to 0 or $\pi$, depending on whether the relative refractive index at the reflection, $n_2/n_1$, is bigger or smaller than 1. Since the intensity is proportional to the square modulus of the electric field,

$$I_{out} \propto |E_{out}|^2 = E^*_{out} E_{out} \tag{2.32}$$

The output intensity will be

$$I_{out} = I_0 \cos^2\left(\frac{\delta}{2}\right) \tag{2.33}$$

This means that there will be some phases at which it is possible to obtain the maximum intensity, and some other phases at which the output intensity will be equal to zero. These phases differences are

$$\begin{aligned} \delta_{\max} &= \frac{4\pi}{\lambda}\Delta L(+\pi) = 2m\pi \\ \delta_{\min} &= \frac{4\pi}{\lambda}\Delta L(+\pi) = (2m+1)\pi \end{aligned} \tag{2.34}$$

where the terms $+\pi$ are added is there is a phase shift at the first reflection, i.e. if $\delta_{\text{ref}} = \pi$.

The light from the QD goes through an high power polarization maintaining (pm) single mode fiber. After a mirror the beam is sent through a 50:50 beamsplitter, where the beam is split into two parts. Then two retroreflectors are used to send back the two beams into the beamsplitter, where they overlap again. Here they interfere, and then the beam coming from this interference is coupled, using two lenses, into another high power polarization maintaining single mode fiber. In this way two perfectly overlapped beams are obtsined. After the fiber a power meter is used, in order to see the intensity of the resulting beam.

One of the two retroreflectors is mounted on a computer controlled translation stage which has a maximum length of 50 cm. The other one is mounted on a mirror mount, mounted on another translation stage with differential micrometric screws. Having all these degrees of freedom allows to perfectly overlap the two beams, and obtain the same coupling efficiency into the fibre. The position along the direction of propagation of the

beam is piezo controlled.
Once the interferometer was mounted it was also tested, verifying that was working properly. We made sure that the coupling efficiency into the fibre of the translation stage mounted arm was the same at the shortest and longest distances. Then we also made sure that the coupling efficiencies of the two arms were the same. We obtained 60 % of coupling efficiency for each arm.
We first tested the interferometer alignment putting the two arms at almost the same distance, and varying the phase difference using the piezo. In this way we obtained, as we expected, an interference pattern. For this measurement we used a low power laser.

If the photons are emitted with a line bandwidth $\Delta\omega = \omega_2 - \omega_1$, the coherence time is defined as

$$\tau_c = \frac{2\pi}{\Delta\omega} \tag{2.35}$$

in fact in a time $\tau$ the phase will change of a quantity $\Delta\omega\tau$, and there will be an uncertainty on the phase. The coherence time is the time interval when this difference is equal to $2\pi$. From $\tau_c$ the coherence length of the photons can be calculated. This is related to the *first order correlation function* $g^{(1)}(\tau)$. Differently from the second order coherence function, which looked at the intensity correlation, this parameter investigates the correlation between the amplitude of two electromagnetic fields at different time intervals. In classical terms it is defined as

$$g^{(1)}(\mathbf{r}_1, t_1; \mathbf{r}_2, t_2) = \frac{|\,\langle \mathbf{E}(\mathbf{r}_1, t)\mathbf{E}(\mathbf{r}_2, t)\rangle\,|}{\left[\langle|\mathbf{E}(\mathbf{r}_1, t)|^2\rangle\,\langle|\mathbf{E}(\mathbf{r}_2, t)|^2\rangle\right]^{\frac{1}{2}}} \tag{2.36}$$

As in the case of the second order correlation function, if stationary states are considered $g^{(1)}(\tau)$ will only depend on the time difference $\tau = t_2 - t_1$. The first order coherence function can be written as

$$g^{(1)}(\tau) = \frac{\langle E^*(t)E(t+\tau)\rangle}{\langle|E(t)|^2\rangle} \tag{2.37}$$

If the electric field has a constant amplitude $E_0$ and a central frequency $\omega_0$ it can be written as

$$E(t) = E_0 e^{-i(\omega_0 t + \phi(t))} \tag{2.38}$$

where $\phi$ is the phase. Then $g^{(1)}(\tau)$ can be calculated:

$$\begin{aligned} g^{(1)}(\tau) &= \frac{\langle E^*(t)E(t+\tau)\rangle}{\langle|E(t)|^2\rangle} = \\ &= \frac{\langle E_0^* e^{i(\omega_0 t+\phi(t))} E_0 e^{-i(\omega_0(t+\tau)+\phi(t+\tau))}\rangle}{\langle|E(t)|^2\rangle} = \\ &= e^{-i\omega_0\tau}\,\langle e^{i\phi(t)} e^{i\phi(t+\tau)}\rangle \end{aligned} \tag{2.39}$$

The final result gives an oscillatory part and an amplitude which depends on the phases at 0 and $\tau$.
Three different cases can be easily seen:

- If $\tau = 0$ then $|g^{(1)}(\tau = 0)| = 1$.

- If $0 < \tau \ll \tau_c$ then $|g^{(1)}(\tau)| \approx 1$ and $\phi(t+\tau) - \phi(t) \approx 0$.
- If $\tau \gg \tau_c$ then $|g^{(1)}(\tau)| \to 0$.

The shape of the correlation function depends on the shape of the emission line. For example, if a shape with a Lorentzian broadening is considered, $g^{(1)}(\tau)$ can be written as

$$g^{(1)}(\tau) = e^{-i\omega_0\tau} e^{-|\tau|/\tau_c} \tag{2.40}$$

With a Michaleson interferometer the visibility can be calculated looking at the fringe intensities, and this is equal to calculate the absolute value of $g^{(1)}(\tau)$ [61].

$$V = \frac{I_{\max} - I_{\min}}{I_{\max} + I_{\min}} = |g^{(1)}(\tau)| \tag{2.41}$$

In this case $\tau = 2\Delta L/c$, where $\Delta L$ is the length difference between the two arms of the interferometer.

After testing the interferometer the measurement of the coherence length of the photons emitted by the single quantum dot was ready to be made. With a script the translation stage was moved, and for every positions the voltage applied to the piezo was changed. In this way the piezo changes its dimension, and consequently also the phase difference of the equation 2.33 changes. This means that varying the applied voltage of the piezo an interference pattern can be seen. This script records the maximum and the minimum intensities of these patterns. At the end it calculates the visibility for every peak as in equation 2.41, and calculates the average between all the obtained visibilities. As can be easily seen, a perfect interference between two sources is obtained when $V = 1$.
The visibility is related to the first order correlation function $g^{(1)}(\tau)$, and then to the coherence time $\tau_c$.
The output electromagnetic field can be written as

$$E_{out}(t) = \frac{1}{\sqrt{2}}\big(E(t) - E(t+\tau)\big) \tag{2.42}$$

where the minus sign is due to the reflection at the beamsplitter, and then a phase shift equal to $\pi$ and a term $e^{i\pi} = -1$. The $1/\sqrt{2}$ term comes from the 50:50 beamsplitter. The intensity will be

$$\begin{aligned} I_{out} &\propto \langle E^*_{out}(t) E_{out}(t)\rangle = \\ &\vdots \\ &= \frac{1}{2}\Big( \langle E^*(t)E(t)\rangle + \langle E^*(t+\tau)E(t+\tau)\rangle - \\ &- \langle E^*(t)E(t+\tau)\rangle - \langle E^*(t)E(t+\tau)\rangle \Big) \end{aligned} \tag{2.43}$$

If the average intensity is constant in time the first two terms are the same, while the last two terms are one the complex conjugate of the other one. The intensity can be written as

$$\begin{aligned} I_{out} &\propto \frac{1}{2}\Big(2\left\langle E^*(t)E(t)\right\rangle - 2\Re\big(\left\langle E^*(t)E(t+\tau)\right\rangle\big)\Big) = \\ &= \left\langle E^*(t)E(t)\right\rangle \Big[1 - \Re\Big(\frac{\left\langle E^*(t)E(t+\tau)\right\rangle}{\left\langle E^*(t)E(t)\right\rangle}\Big)\Big] \end{aligned} \tag{2.44}$$

The output intensity can be finally written as

$$I_{\text{out}} = I(\tau) = I_0\Big[1 - \Re\big(g^{(1)}(\tau)\big)\Big] \tag{2.45}$$

With the maximum and minimum intensity equal to

$$I_{\text{max,min}} = I_0\Big[1 \pm |g^{(1)}(\tau)|\Big] \tag{2.46}$$

the visibility is exactly the first order correlation function:

$$V = \frac{I_{\text{max}} - I_{\text{min}}}{I_{\text{max}} + I_{\text{min}}} = |g^{(1)}(\tau)| \tag{2.47}$$

With a constant average intensity, the visibility V is only function of the time difference between the two paths $\tau$.
The value of the visibility was supposed to be recorded for every position of the translation stage, and then plotted versus the length difference of the two arms. Since the emitted photons have a finite coherence length, when the length difference between the two arms becomes larger than the coherence length the visibility decreases, until the photons don't interfere anymore and the visibility becomes equal to 0. Since from equation 2.40 the first order correlation function has an exponential decrease with the increasing of $\tau$, the coherence length is then calculated as the characteristic time $\tau$ of an exponential fit $e^{-t/\tau}$.
Unfortunately, due to many technical problems which occurred during the thesis, it was not possible to measure the coherence length of the emitted photons before the end of the project.

# Chapter 3

# Experimental results

## 3.1 A single Quantum Dot spectrum

In order to characterize the investigated sample, many different quantum dots of the sample were excited, trying to find which ones among all the dots had the best emission properties. The quantum dot with the required emission properties must have well-defined characteristic emission lines (exciton and biexciton), and must not show much background noise.
During the scanning procedure the sample was moved with the piezo controller until the spot of the beam was above the quantum dot. Then, if the characteristic emission lines of the dot (exciton and biexciton lines) were observed, the emission rate of these lines was optimized. Looking at the intensity of the peaks the position of the sample was first moved with the piezo controller, and then the focus of the laser beam was changed moving the telescope lens with a differential micrometric screw.

This procedure was repeated multiple times in order to get the maximum emission rate. Some emission spectra from the considered nanowire quantum dot can be seen in Figure 3.1, acquired with the spectrometer and different laser powers. These spectra were obtained with an above band excitation, using a 635 nm continouos wave laser, with an integration time of 0.3 s. The exciton and the biexciton lines can be seen, while the line on the left is due to some light scattering from the laser. As previously explained, with the above band excitation a large amount of carriers is produced, and this quantity increases as the excitation power is increased. This fact produces a relevant background, especially with high excitation powers.

As explained in the section 1.3.1, the exciton and biexciton lines show different behaviours for an increasing excitation power, under above band excitation. In particular in a logarithmic scale the exciton line shows a linear dependence while the biexciton line shows a quadratic one. If the intensities of the lines were plotted versus the excitation power one should be able to distinguish the different nature of the two lines. The results can be seen in Figure 3.2. The two colors shows the number of counts for each line. The plot is made taking spectra for different excitation powers, and using a ROOT script the background is removed (as can be seen in figure 3.3), the two peaks are fitted with a gaussian function and the integral of the function is calculated. Then the data for each

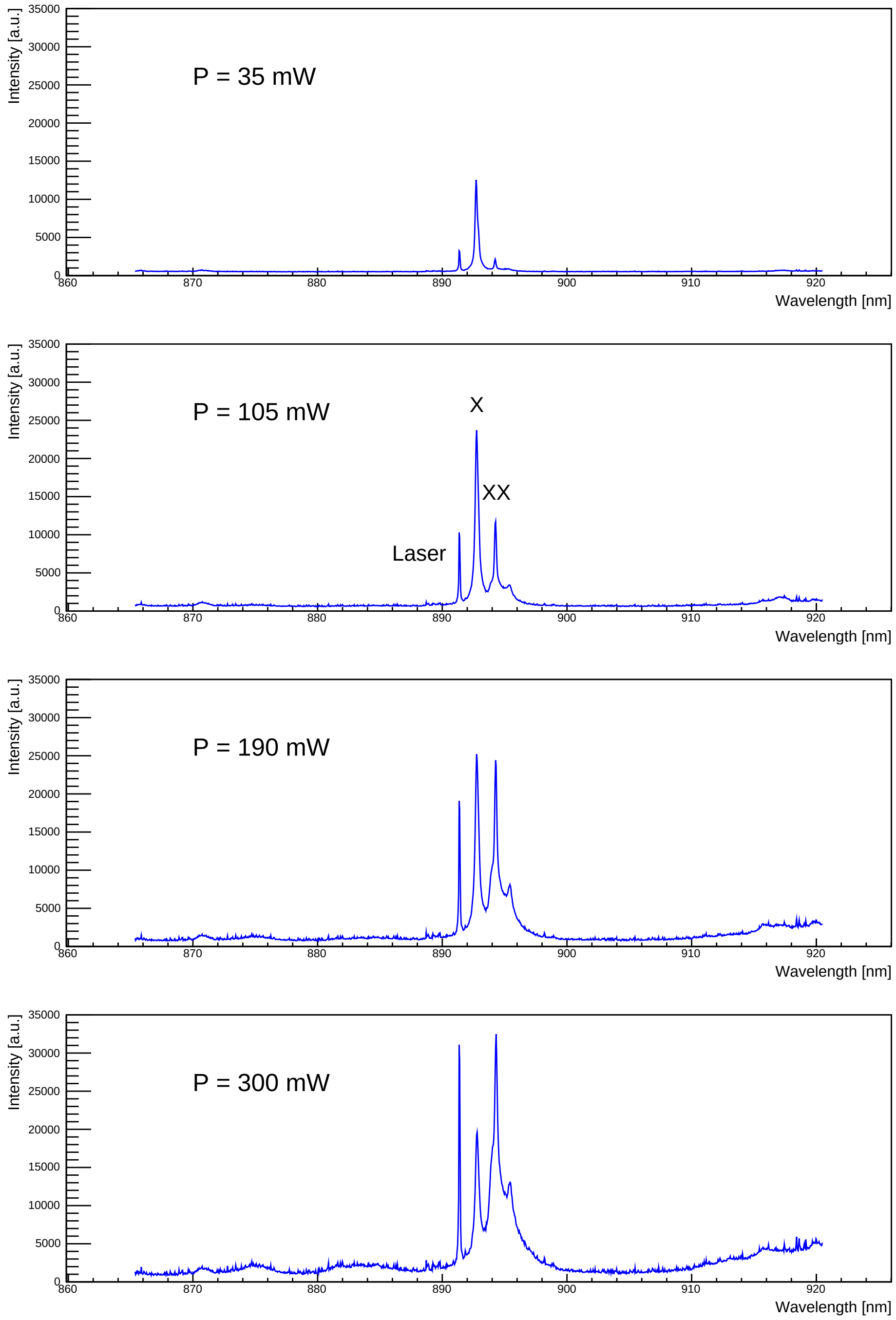

Figure 3.1: Spectra of the considered nanowire quantum dot, under above band excitation, with a 635 nm continuous wave laser and different excitation powers. The exciton and biexciton lines can be seen. The line on the left is a line due to some light scattering from the laser, while the one on the right probably corresponds to another excited state. The exciton and the biexciton lines show different behaviours when the excitation power is varied. Due to the high efficiency of the above band excitation, with increasing powers a large amount of carriers is created, and this contributes to a relevant background.

line are plotted in a double logarithmic scale.

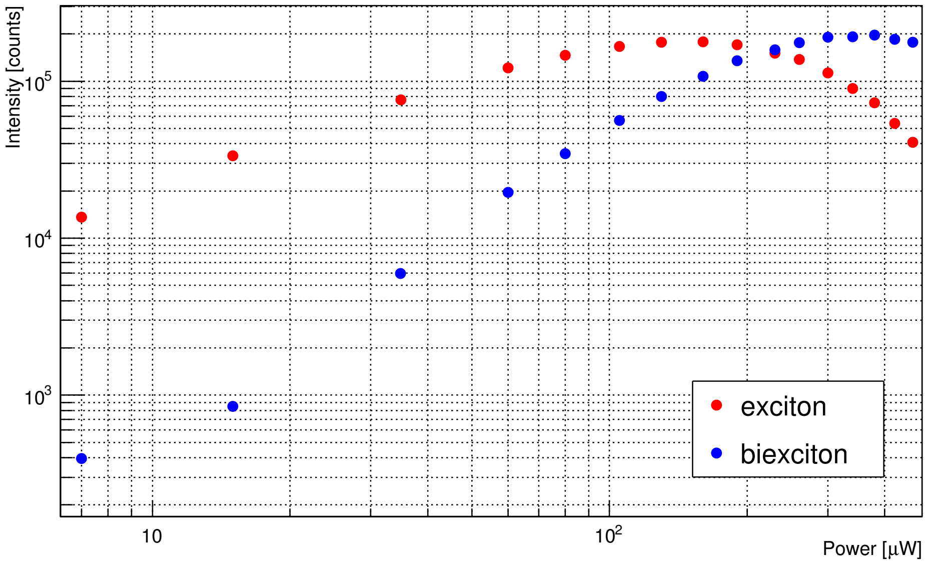

Figure 3.2: Power dependence of the intensity of the exciton and biexciton lines under above band excitation, with a 635 nm laser. Fitting the data with the function 3.1 we notice that the exciton line shows linear slope, while the biexciton one a quadratic slope. Increasing the excitation power they saturate, because other excitation processes start arising.

It can be seen that the two lines show different slopes. The two sets of data for can be fitted for low powers (i.e. when there is still no saturation) with the function

$$\log(I) = k\log(P) + c \tag{3.1}$$

where $I$ is the intensity of the peak and $P$ the excitation power. In the case of the biexciton line the first point is removed, because when the power was too low the line was submerged in the background noise. The following slopes for the two lines are obtained:

$$k_{\mathrm{X}} = 1.02 \pm 0.04\, \mu W^{-1}$$

for the exciton, and

$$k_{\mathrm{XX}} = 2.09 \pm 0.06\, muW^{-1}$$

for the biexciton.

In first case the compatibility with the expected value is equal to 0.5, while in the second case is equal to 1.5. In both cases these are good compatibilities. It can be said that these lines are respectively the exciton and the biexciton line. When the excitation power is increased the counts in the biexciton line become higher than the ones in the exciton line, which start decreasing the counts. In fact photons by the biexciton will be created once the exciton level is saturated [39]. If the excitation power is even more increased, also the biexciton line start decreasing its intensity, because other excitation processes start arising.

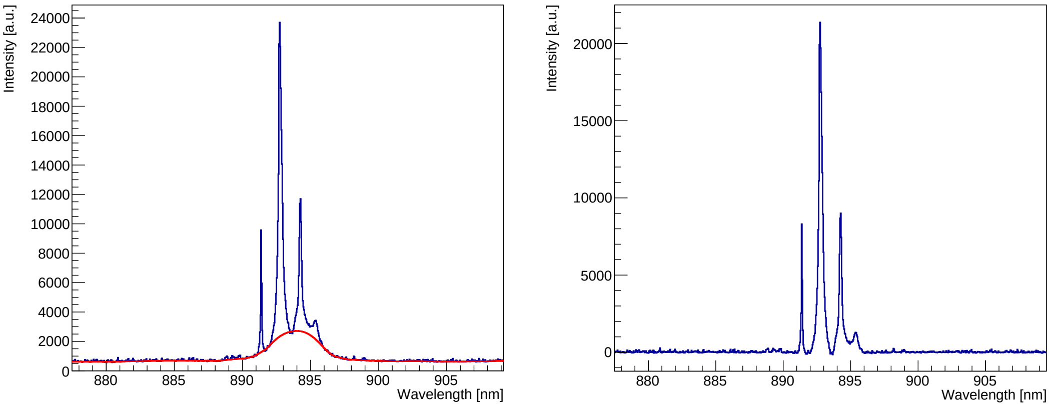

Figure 3.3: Example of spectrum of the quantum dot with above band excitation (in this case with a power of 105 mW) before and after removing the background. This procedure was useful to estimate the number of counts under the emission lines and get the figure 3.2. It was also useful to better calculate the FWHM of the peaks.

Looking at the width of the emission lines it is possible to give and estimation of the excited state lifetime. As explained in section 1.2, if $\Gamma$ is the full width at half-maximum of the emission line, it is linked to the natural lifetime of the state by the relation $\Gamma = \hbar/\tau$. Therefore after removing the background signal it was possible to measure the full width at half-maximum and then estimate the lifetimes of the excited states, which gave for both the exciton and the biexciton a lifetime shorter than 5 ps. However as described in literature [62], the measured lifetime for excited states in InAs/GaAs quantum dots is of the order of few nanoseconds. Therefore there are some processes that lead to such a broad distribution. One reason could be the non resonant excitation that we are using for this measurement. Moreover it must be taken into account that if the beam is not perfectly focused into the fiber, one would get a broadening of the peak.

## 3.2 Measurements of $g^{(2)}(\tau)$

### 3.2.1 Exciton autocorrelation

Some measurements of the autocorrelation between the exciton photons are taken, under continuous wave above band laser excitation, with a wavelength $\lambda = 635$ nm. One example of these measurements can be seen in figure 3.4. The output of the self-made spectrometer was coupled in a single mode fibre, and the beam was split by a fiber beam splitter. The two beams are then sent into two different APDs, and the signals are sent to a Time to Digital Converter. As can be seen in figure 3.4, the function shows the typical shape of a Sub-Poissonian source. The minimum value of the second order correlation function is :

$$g^{(2)}(0) \approx 0.1 \tag{3.2}$$

Since this value is lower than one, the excited single semiconductor quantum dot can be considered a non classical light source.

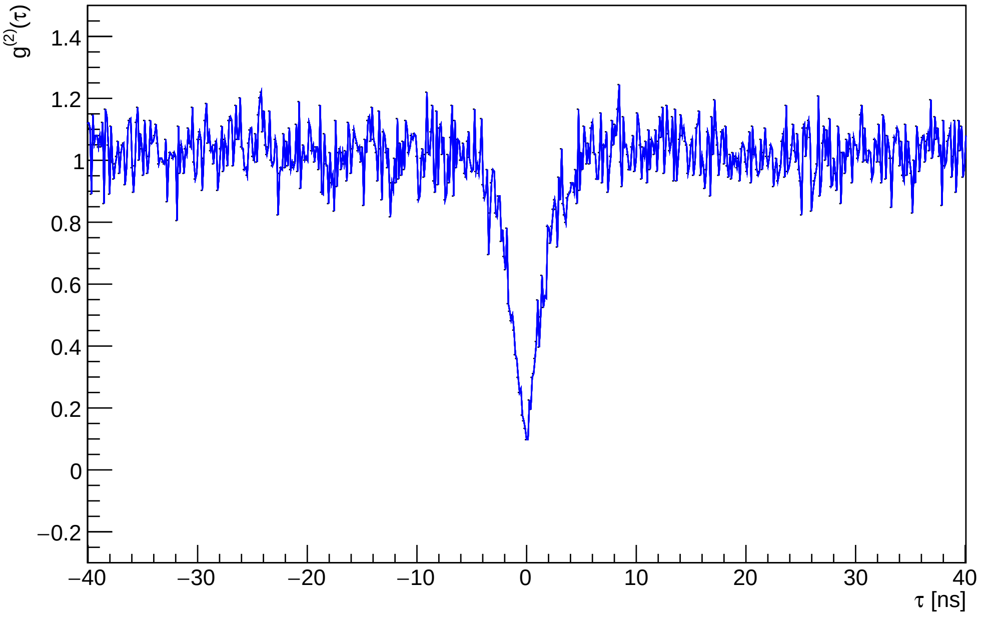

Figure 3.4: Measurement of the autocorrelation function of the exciton photons emitted by the quantum dot, under above band excitation with 635 nm wavelength continuous wave laser. As can be seen, the correlation function $g^{(2)}(\tau)$ shows the typical behaviour of a Sub-Poissonian source.

# Chapter 4

# Conclusions

During this thesis project we addressed the complex task to produce and characterize non-classical sources of light. We did a preliminary work to build and test some dedicated set-ups for measuring the quantum nature of the emmitter, which was selected as $\sim 10$ nm InAs quantum dots cooled to 4 K to reduce the thermal noise. The size was selected to be less than the excitonic Bohr radius (which is 35.5 nm for bulk InAs) to be in the strong confinement regime and obtain better excitonic and biexcitonic emission.

We have developed an apparatus composed by different devices for the characterization of the emission of a single semiconductor quantum dot. With such apparatus, it is possible to excite the quantum dot from above, collect the emitted light with a high NA lens and see its emission spectrum with a commercial spectrometer. In this way it is possible to have a quick overview of the spectra of the excited quantum dot, and check if it is emitting properly. The main emission lines of the quantum dots, corresponding to the exciton and the biexciton lines, have been observed under above band excitation.

Moreover, the spectrum can also be observed using a self-made spectrometer. This spectrometer is especially useful when a separation of the path of the emitted photons is needed. With a prism after the diffraction grating, it is possible to separate the exciton photons from the biexciton photons. In this way it is possible to make important measurements, such as the auto-correlation of the exciton and biexciton photons, and the cross-correlation between the exciton and biexciton photons. These measurements prove that if cooled down to low temperatures (4 K) and under a proper excitation, a single semiconductor quantum dot can be considered a single photon source. This emission regime cannot be reached with classical sources, so a single quantum dot can be an emitter of quantum light. Moreover with the self-made spectrometer the emitted photons are coupled into fibers, and consequently the light can be easily sent to other parts of the experimental setup, which will be built in a future work.

An important parameter for the characterization of a photon source is its coherence length. Since all quantum photonics is based upon Hong-Ou-Mandel interference (which requires indistinguishable photons in order to happen) it is important to have photons with a long coherence length. For this reason a Michaelson interferometer has been built, in order to measure the coherence length of the emitted photons. Unfortunately, at present the coherence length measurement is not yet available.

All the measurements have been taken under above band continuous wave excitation. As previously said in section 1.3.1, this kind of excitation has a great efficiency, but due to the background noise and the time jitter caused by the phonon scattering, the emitted photons have poor properties (e.g. short coherence length and low indistinguishability), and are not suitable for applications in quantum information protocols. What is needed is a resonant excitation of the single semiconductor quantum dot. This is the reason why during the project a pulse stretcher has been designed and built. Starting from a femtosecond Ti:Sapphire pulsed laser, with the pulse stretcher it is possible to easily tune its temporal length by cutting its spectrum with a slit. The goal is to obtain the correct temporal length of the pulse, in order to obtain the *Rabi oscillations* and an optimal excitation probability, as can be seen for the biexciton photon in figure 4.1 (from [63]). The longest pulse obtained with the stretcher is a 5.4 ps long pulse, which is long enough to obtain Rabi oscillations.

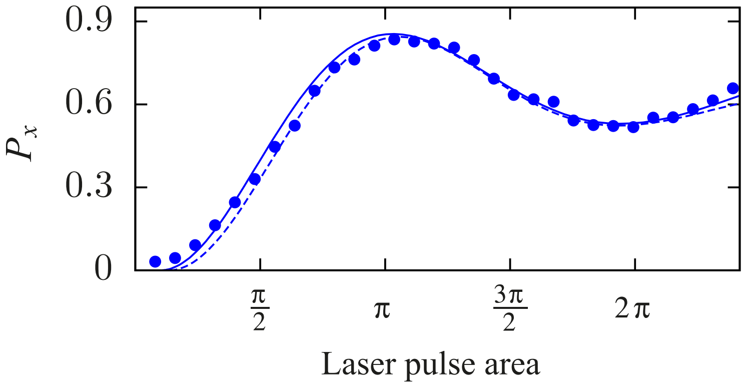

Figure 4.1: Example of Rabi oscillations, with experimental data compared to theoretical predictions, from [63]. $P_x$ is the emission probability of an exciton photon as function of the laser pulse area. For a certain pulse area ($\pi$ pulse) the emission probability is maximized.

The further developments of the apparatus should include first of all the implementation of the Michaelson interferometer to the experimental setup. Thanks to this device a fundamental parameter for quantum photonics can be measured, i.e. the coherence length of the emitted photons.

Then the setup can be adapted to measure other important quantities, such as the autocorrelation of the biexciton photons and the cross correlation between the exciton and biexciton photons. In this way a deeper understanding of the emission and the temporal ordering of the emission cascade of the single quantum dot can be achieved, obtaining a more complete characterization of the used device.

Finally, the pulse stretcher should be also added to all the experimental setup. Using it, it should be possible to obtain a resonant excitation of the single quantum dot. Then, all the measurement previously done with above band excitation can be made with resonant excitation. The results obtained with these two methods can be compared, measuring the improvements that come with the resonant excitation.

Once the resonant excitation is achieved, it will be possible to measure the indistinguishability property of the emitted photons, through the Hong-Ou-Mandel interference, and

it will be possible to decide whether the used quantum dots are suitable for quantum information applications.
Another goal is to obtain with the help of the pulse stretcher the two-photons resonant excitation. This kind of excitation is useful when a generation of entangled photon pairs is needed.

After all these goals are achieved the setup can be used with any kind of quantum dots, hence new configurations can be explored and fully characterized (different compositions of quantum dots or different geometries, such as using other kind of cavities coupled with the quantum dots). Moreover the feasibility of their use in different quantum information protocols (e.g. how good are the Bells states that can be prepared of quantum dots, or the quality of quantum teleportation) can be proved, leading maybe one day to their implementation on a big scale also in these fields.

# Appendix A

# Fock and coherent states

The quantum Hamiltonian of the electromagnetic field can be written as a sum of an infinite number of not coupled harmonic oscillators [64]

$$\hat{H} = \sum_{\mathbf{k}} \sum_{s} \Big( \frac{\hat{p}_{\mathbf{k},s}}{2} + \frac{1}{2}\omega_k^2 \hat{q}_{\mathbf{k},s}^2 \Big) \tag{A.1}$$

where $\hat{p}$ and $\hat{q}$ are respectively the momentum and the position, $\omega$ is the angular frequency of the harmonic oscillator, $\mathbf{k}$ is the wave vector, s is the polarization. If we define the *creation* and *annihilation* operators $\hat{a}^\dagger$ and $\hat{a}$ as

$$\hat{a}_{\mathbf{k},s}^\dagger = \sqrt{\frac{\omega_k}{2\hbar}} \Big( \hat{q}_{\mathbf{k},s} - \frac{i}{\omega_k} \hat{p}_{\mathbf{k},s} \Big) \tag{A.2}$$

$$\hat{a}_{\mathbf{k},s} = \sqrt{\frac{\omega_k}{2\hbar}} \Big( \hat{q}_{\mathbf{k},s} + \frac{i}{\omega_k} \hat{p}_{\mathbf{k},s} \Big) \tag{A.3}$$

which satisfy the commutation rule

$$[\hat{a}_{\mathbf{k},s}, \hat{a}_{\mathbf{k}',s'}^\dagger] = \delta_{\mathbf{k},\mathbf{k}'} \delta_{s,s'}$$

we can write the Hamiltonian as

$$\hat{H} = \sum_{\mathbf{k}} \sum_{s} \hbar\omega_k \Big( \hat{a}_{\mathbf{k},s}^\dagger \hat{a}_{\mathbf{k},s} + \frac{1}{2} \Big) \tag{A.4}$$

The creation and annihilation operators act in the Fock space, which is the Hilbert space of the "number representation", obtained as

$$\mathcal{F} = \mathcal{H}_0 \oplus \mathcal{H}_1 \oplus \cdots \oplus \mathcal{H}_n = \bigoplus_n \mathcal{H}_n \tag{A.5}$$

where

$$\mathcal{H}_n = \mathcal{H} \otimes \mathcal{H} \cdots \otimes \mathcal{H} = \mathcal{H}^{\otimes n} \tag{A.6}$$

is the Hilbert space of $n$ identical photons, obtained as the tensor product of $n$ single particle Hilbert spaces.

A typical Fock state is

$$|n_{\mathbf{k},s} \dots n_{\mathbf{k}',s'} \dots n_{\mathbf{k}'',s''}\rangle \tag{A.7}$$

which means that there are $n_{\mathbf{k},s}$ photons with wavevector $\mathbf{k}$ and polarization s, $n_{\mathbf{k}',s'}$ photons with wavevector $\mathbf{k'}$ and polarization s', and so on.
The creation and annihilation operators act on a generic Fock state $|n\rangle$ as:

$$\hat{a}^\dagger |n\rangle = \sqrt{n+1}\,|n+1\rangle \tag{A.8}$$

$$\hat{a}\,|n\rangle = \sqrt{n}\,|n-1\rangle \tag{A.9}$$

that means that Fock states are not eigenvalues of creation and annihilation operators.If we define the *number operator* $\hat{N}_{\mathbf{k},s}$ as

$$\hat{N}_{\mathbf{k},s} = \hat{a}^\dagger_{\mathbf{k},s}\hat{a}_{\mathbf{k},s} \tag{A.10}$$

which counts the number of particles in the state $|\mathbf{k}s\rangle$, we obtain the subsequent eigenvalue equation

$$\hat{N}_{\mathbf{k},s}\,|\dots n_{\mathbf{k},s}\dots\rangle = n_{\mathbf{k},s}\,|\dots n_{\mathbf{k},s}\dots\rangle \tag{A.11}$$

Which means that the Fock states are the eigenstates of the number operator, and the relative eigenvalue is equal to the number of photons in the $|n\rangle$ state.
The Hamiltonian of the electromagnetic field can be written as

$$\hat{H} = \sum_{\mathbf{k}}\sum_{s} \hbar\omega_k\Big(\hat{N}_{\mathbf{k},s} + \frac{1}{2}\Big) \tag{A.12}$$

Where the second term is the energy of the vacuum state. This means that the energy of vacuum state is not equal to zero.
The electric and magnetic fields can be quantized substituting the classical amplitudes $a_{\mathbf{k}s}$ and $a^*_{\mathbf{k}s}$ with the annihilation and creation operator. In this way we obtain the subsequent fields:

$$\hat{E}(\mathbf{r},t) = i\sum_{\mathbf{k}}\sum_{s}\sqrt{\frac{\hbar\omega_k}{2\epsilon_0 V}}[\hat{a}_{\mathbf{k},s}e^{i(\mathbf{k}\cdot\mathbf{r}-\omega_k t)} - \hat{a}^\dagger_{\mathbf{k},s}e^{-i(\mathbf{k}\cdot\mathbf{r}-\omega_k t)}]\epsilon_{\mathbf{k},s} \tag{A.13}$$

$$\hat{B}(\mathbf{r},t) = i\sum_{\mathbf{k}}\sum_{s}\sqrt{\frac{\hbar\omega_k}{2\epsilon_0 V}}[\hat{a}_{\mathbf{k},s}e^{i(\mathbf{k}\cdot\mathbf{r}-\omega_k t)} - \hat{a}^\dagger_{\mathbf{k},s}e^{-i(\mathbf{k}\cdot\mathbf{r}-\omega_k t)}]i\frac{\mathbf{k}}{|\mathbf{k}|}\times\epsilon_{\mathbf{k},s} \tag{A.14}$$

If we consider a perfect linear polarized monochromatic wave (and semplify the notation substituting $\hat{a}_{\mathbf{k}s}$ and $\hat{a}^\dagger_{\mathbf{k}s}$ with $\hat{a}$ and $\hat{a}^\dagger$ we can write the following electric field :

$$\hat{E}(\mathbf{r},t) = i\sqrt{\frac{\hbar\omega}{2\epsilon_0 V}}[\hat{a}e^{i(\mathbf{k}\cdot\mathbf{r}-\omega t)} - \hat{a}^\dagger e^{-i(\mathbf{k}\cdot\mathbf{r}-\omega t)}]\epsilon \tag{A.15}$$

where $\omega = \omega_k = c|\mathbf{k}|$.
If we have a Fock state with $n$ photons it is given by

$$|n\rangle = \frac{1}{\sqrt{n!}}(\hat{a}^\dagger)^n\,|0\rangle \tag{A.16}$$

but if we calculate the expectation value of the electric field in this state is easy to see that

$$\langle n|\hat{E}(\mathbf{r},t)|n\rangle = 0 \tag{A.17}$$

for every value of n. However if we calculate the expectation value

$$\langle n|\hat{E}(\mathbf{r},t)^2|n\rangle = \frac{\hbar}{\epsilon_0 V}\Big(n+\frac{1}{2}\Big) \tag{A.18}$$

The expectation value of the intensity of the field is always different from zero, even for the vacuum state.
This weird result is due to the fact that the expectation value is calculated in a Fock state, which has a fixed number of photons. But usually this number in a radiation field is not fixed. For example, the photon emission of a laser operating above the threshold is well described by a coherent state $|\alpha\rangle$, introduced by Roy Glauber in 1963 [65]. By definition, coherent states are the eigenstates of the annihilation operator

$$\hat{a}\,|\alpha\rangle = \alpha\,|\alpha\rangle \tag{A.19}$$

These states are normalized

$$\langle\alpha|\alpha\rangle = 1 \tag{A.20}$$

They have complex eigenvalues $\alpha = |\alpha|e^{i\theta}$. Coherent states have not a fixed number of photons, that means that they are not eigenstates of the number operator. They can be written as function of the Fock states, as

$$|\alpha\rangle = e^{-\frac{|\alpha|^2}{2}}\sum_{n=0}^{\infty}\frac{\alpha^n}{\sqrt{n!}}\,|n\rangle \tag{A.21}$$

and is easy to find that

$$N = \langle\alpha|\hat{N}|\alpha\rangle \tag{A.22}$$

Where N is the average number of photons in the coherent state [64]. If we calculate the expectation value of the electric field on a coherent state what we get is

$$\langle\alpha|\hat{E}(\mathbf{r},t)|\alpha\rangle = -\sqrt{\frac{2N\hbar\omega}{\epsilon_0 V}}\sin(\mathbf{k}\cdot\mathbf{r}-\omega t+\theta)\epsilon \tag{A.23}$$

while the expectation value of $\hat{E}^2(\mathbf{r}t)$ is

$$\langle\alpha|\hat{E}^2(\mathbf{r},t)|\alpha\rangle = -\frac{2N\hbar\omega}{\epsilon_0 V}\sin^2(\mathbf{k}\cdot\mathbf{r}-\omega t+\theta) \tag{A.24}$$

What we get is the classic electric field. This suggests that the coherent state is the natural connection between the classical electric field and the quantum electric field.

# Bibliography

[1] Christof P. Dietrich, Andrea Fiore, Mark G. Thompson, Martin Kamp, and Sven Höfling. GaAs integrated quantum photonics: Towards compact and multi-functional quantum photonic integrated circuits. *Laser & Photonics Reviews*, 10(6):870–894, sep 2016.

[2] Andrei Faraon, Arka Majumdar, Dirk Englund, Erik Kim, Michal Bajcsy, and Jelena Vučković. Integrated quantum optical networks based on quantum dots and photonic crystals. *New Journal of Physics*, 13(5):055025, may 2011.

[3] Igor A. Khramtsov, Mario Agio, and Dmitry Yu. Fedyanin. Dynamics of single-photon emission from electrically pumped color centers. *Physical Review Applied*, 8(2), aug 2017.

[4] John N.; Palomares Emilio Albero, Josep; Clifford. Quantum dot based molecular solar cells. *Coordination Chemistry Reviews*, 263-264, 03 2014.

[5] Ranjana; Kumar Shiv Sharma, Darshan; Jha. Quantum dot sensitized solar cell: Recent advances and future perspectives in photoanode. *Solar Energy Materials and Solar Cells*, 155, 10 2016.

[6] J. E.; Wood V.; Bulović V.; Bawendi M. G. Caruge, J. M.; Halpert. Colloidal quantum-dot light-emitting diodes with metal-oxide charge transport layers. *Nature Photonics*, 2, 2008.

[7] C. Santori, D. Fattal, J. Vuckovic, G. S. Solomon, and Y. Yamamoto. Indistinguishable photons from a single-photon device. In *Proc. QELS. Postconference Digest Quantum Electronics and Laser Science*, pages 2 pp.–, June 2003.

[8] N. Akopian, N. H. Lindner, E. Poem, Y. Berlatzky, J. Avron, D. Gershoni, B. D. Gerardot, and P. M. Petroff. Entangled photon pairs from semiconductor quantum dots. *Phys. Rev. Lett.*, 96:130501, Apr 2006.

[9] C. Tablero. Quantum dot energy levels and spectrum for different geometries. *Journal of Applied Physics*, 106, 2009.

[10] Ivan V Markov. *Crystal Growth for Beginners.* WORLD SCIENTIFIC, aug 2003.

[11] Alberto Pimpinelli and Jacques Villain. *Physics of Crystal Growth.* Collection Alea-Saclay: Monographs and Texts in Statistical Physics. Cambridge University Press, 1998.

[12] Seungwon Lee, Olga L. Lazarenkova, Paul von Allmen, Fabiano Oyafuso, and Gerhard Klimeck. Effect of wetting layers on the strain and electronic structure of InAs self-assembled quantum dots. *Physical Review B*, 70(12), sep 2004.

[13] A.; Heitz R.; Timm R.; Dahne M.; Temko Y.; Suzuki T.; Jacobi K. Eisele, H.; Lenz. Change of inas/gaas quantum dot shape and composition during capping. *Journal of Applied Physics*, 104, 2008.

[14] Charles M. Santori. *Generation of nonclassical light using semiconductor quantum dots*. PhD thesis, stanford university, 2002.

[15] Takaaki Mano, Katsuyuki Watanabe, Shiro Tsukamoto, Hiroshi Fujioka, Masaharu Oshima, and Nobuyuki Koguchi. New self-organized growth method for ingaas quantum dots on gaas(001) using droplet epitaxy. *Japanese Journal of Applied Physics*, 38(9A):L1009, 1999.

[16] Akos Nemcsics. Quantum dots prepared by droplet epitaxial method. In *Quantum Dots - Theory and Applications*. InTech, sep 2015.

[17] Neul Ha, Xiangming Liu, Takaaki Mano, Takashi Kuroda, Kazutaka Mitsuishi, Andrea Castellano, Stefano Sanguinetti, Takeshi Noda, Yoshiki Sakuma, and Kazuaki Sakoda. Droplet epitaxial growth of highly symmetric quantum dots emitting at telecommunication wavelengths on InP(111)a. *Applied Physics Letters*, 104(14):143106, apr 2014.

[18] H Heidemeyer, C Müller, and O.G Schmidt. Highly ordered arrays of in(ga)as quantum dots on patterned gaas(001) substrates. *Journal of Crystal Growth*, 261(4):444 – 449, 2004.

[19] J. Martín-Sánchez, G. Muñoz-Matutano, J. Herranz, J. Canet-Ferrer, B. Alén, Y. González, P. Alonso-González, D. Fuster, L. González, J. Martínez-Pastor, and F. Briones. Single photon emission from site-controlled InAs quantum dots grown on GaAs(001) patterned substrates. *ACS Nano*, 3(6):1513–1517, may 2009.

[20] Juha Tommila, Christian Strelow, Andreas Schramm, Teemu V Hakkarainen, Mihail Dumitrescu, Tobias Kipp, and Mircea Guina. The influence of temperature on the photoluminescence properties of single InAs quantum dots grown on patterned GaAs. *Nanoscale Research Letters*, 7(1), jun 2012.

[21] J. Canet-Ferrer, G. Munoz-Matutano, J. Herranz, D. Rivas, B. Alen, Y. Gonzalez, D. Fuster, L. Gonzalez, and J. Martínez-Pastor. Exciton and multiexciton optical properties of single InAs/GaAs site-controlled quantum dots. *Applied Physics Letters*, 103(18):183112, oct 2013.

[22] M.; Sünner T.; Huggenberger A.; Wiener D.; Reitzenstein S.; Kamp M.; Höfling S.; Forchel A. Schneider, C.; Strauß. Lithographic alignment to site-controlled quantum dots for device integration. *Applied Physics Letters*, 92, 2008.

[23] Jun Tatebayashi, Masao Nishioka, Takao Someya, and Yasuhiko Arakawa. Area-controlled growth of InAs quantum dots and improvement of density and size distribution. *Applied Physics Letters*, 77(21):3382–3384, nov 2000.

[24] Luca Francaviglia, Yannik Fontana, and Anna Fontcuberta i Morral. Quantum Dots in Nanowires. In *Semiconductors and Semimetals*, pages 159–184. Elsevier, 2016.

[25] Yang Xu. *Synthesis and characterization of silica coated CdSe/CdS core/shell quantum dots*. PhD thesis, Virginia Tech, 2005.

[26] Thomas Ihn. Envelope functions and effective mass approximation. In *Semiconductor Nanostructures*, pages 53–62. Oxford University Press, nov 2009.

[27] Schulman Joel Bastard Gerald. Wave mechanics applied to semiconductor heterostructures. *Physics Today*, 45, 1992.

[28] Eliana Biolatti, Irene D'Amico, Paolo Zanardi, and Fausto Rossi. Electro-optical properties of semiconductor quantum dots: Application to quantum information processing. *Physical Review B*, 65(7), jan 2002.

[29] Claude Cohen-Tannoudji, Bernard Diu, and Frank Laloe. *Quantum Mechanics, Volume 1*. John Wiley & Sons Inc, 1977.

[30] A. Einstein. Strahlungs-emission und absorption nach der quantentheorie. *Deutsche Physikalische Gesellschaft*, 18, 1916.

[31] Simone Luca Portalupi and Peter Michler. Resonantly excited quantum dots: Superior non-classical light sources for quantum information. In *Quantum Dots for Quantum Information Technologies*, pages 77–121. Springer International Publishing, 2017.

[32] Y. Toda, S. Shinomori, K. Suzuki, and Y. Arakawa. Polarized photoluminescence spectroscopy of single self-assembled inas quantum dots. *Phys. Rev. B*, 58:R10147–R10150, Oct 1998.

[33] E. Moreau, I. Robert, L. Manin, V. Thierry-Mieg, J. M. Gérard, and I. Abram. Quantum cascade of photons in semiconductor quantum dots. *Phys. Rev. Lett.*, 87:183601, Oct 2001.

[34] M. Abbarchi; T. Kuroda; C. Mastrandrea; A. Vinattieri; S. Sanguinetti; T. Mano; K. Sakoda; M. Gurioli. Fine structure splitting of quantum dot excitons: Role of geometry and environment. *Physica E: Low-dimensional Systems and Nanostructures*, 42, 2010.

[35] Gammon, Snow, Shanabrook, Katzer, and Y B Park. Fine structure splitting in the optical spectra of single gaas quantum dots. *Physical review letters*, 76 16:3005–3008, 1996.

[36] J. Seebeck, T. R. Nielsen, P. Gartner, and F. Jahnke. Polarons in semiconductor quantum dots and their role in the quantum kinetics of carrier relaxation. *Phys. Rev. B*, 71:125327, Mar 2005.

[37] E. A. Muljarov and R. Zimmermann. Dephasing in quantum dots: Quadratic coupling to acoustic phonons. *Phys. Rev. Lett.*, 93:237401, Nov 2004.

[38] S. Ates, S. M. Ulrich, S. Reitzenstein, A. Löffler, A. Forchel, and P. Michler. Post-selected indistinguishable photons from the resonance fluorescence of a single quantum dot in a microcavity. *Phys. Rev. Lett.*, 103:167402, Oct 2009.

[39] Ana Predojević. Resonant Excitation and Photon Entanglement from Semiconductor Quantum Dots. In *Engineering the Atom-Photon Interaction*, pages 303–324. Springer International Publishing, 2015.

[40] Edward B. Flagg, Sergey V. Polyakov, Tim Thomay, and Glenn S. Solomon. Dynamics of nonclassical light from a single solid-state quantum emitter. *Phys. Rev. Lett.*, 109:163601, Oct 2012.

[41] Leslie C. Allen. *Optical Resonance and Two-Level Atoms.* DOVER PUBLICATIONS, 1987.

[42] Oliver Benson. *Course of Quantenoptik*, chapter 7, pages 1–16. Humboldt university of Berlin, 2009.

[43] Peter Michler. *Nonclassical Light from Single Semiconductor Quantum Dots*, pages 315–347. Springer Berlin Heidelberg, Berlin, Heidelberg, 2003.

[44] Hans-A. Bachor and Timothy C. Ralph, editors. *A Guide to Experiments in Quantum Optics.* Wiley-VCH Verlag GmbH, jan 2004.

[45] Alan Migdall, Sergey V. Polyakov, Jingyun Fan, and Joshua C. Bienfang, editors. *Single-photon generation and detection.* Number 45 in Experimental methods in the physical sciences. Elsevier/Acad. Press, Amsterdam [u.a.], 2013. Literaturangaben.

[46] Jinhyoung Lee, M. S. Kim, and Časlav Brukner. Operationally invariant measure of the distance between quantum states by complementary measurements. *Phys. Rev. Lett.*, 91:087902, Aug 2003.

[47] C. K. Hong, Z. Y. Ou, and L. Mandel. Measurement of subpicosecond time intervals between two photons by interference. *Phys. Rev. Lett.*, 59:2044–2046, Nov 1987.

[48] Agata M. Brańczyk. Hong-Ou-Mandel Interference. 2017.

[49] Karlheinz Seeger. *Semiconductor Physics.* Springer Berlin Heidelberg, 1991.

[50] Umesh K. Mishra. *Semiconductor Device Physics and Design —— Field Effect Transistors: MOSFET*, volume 10.1007/978-1-4020-6481-4. 2007.

[51] Z. M. Fang, K. Y. Ma, D. H. Jaw, R. M. Cohen, and G. B. Stringfellow. Photoluminescence of InSb, InAs, and InAsSb grown by organometallic vapor phase epitaxy. *Journal of Applied Physics*, 67(11):7034–7039, jun 1990.

[52] PIXIS 400 Datasheet.

[53] Christopher Palmer. *Diffraction Grating Handbook (7th edition)*, pages 20–22. 01 2014.

[54] Christopher Palmer. *Diffraction Grating Handbook (7th edition)*, page 31. 01 2014.

[55] quTAG *qutools* Datasheet.

[56] Malvin Carl Teich Bahaa E. A. Saleh. *Fundamentals of photonics.* Wiley series in pure and applied optics. Wiley, 1st edition, 1991.

[57] C. Hirlimann. Pulsed optics. In *Advanced Texts in Physics*, pages 25–56. Springer New York.

[58] Tobias Huber, Maximilian Prilmüller, Michael Sehner, Glenn S Solomon, Ana Predojević, and Gregor Weihs. Interfacing a quantum dot with a spontaneous parametric down-conversion source. *Quantum Science and Technology*, 2(3):034016, 2017.

[59] Valentina Cesari, Wolfgang Langbein, and Paola Borri. Dephasing of excitons and multiexcitons in undoped and p-doped InAs/GaAs quantum dots-in-a-well. *Physical Review B*, 82(19), nov 2010.

[60] Toshihide Takagahara. Theory of exciton dephasing in semiconductor quantum dots. In *Semiconductor Quantum Dots*, pages 353–388. Springer Berlin Heidelberg, 2002.

[61] Max Born, Emil Wolf, and A. B. Bhatia. *Principles of Optics.* Cambridge University Pr., 2002.

[62] C. Bardot, M. Schwab, M. Bayer, S. Fafard, Z. Wasilewski, and P. Hawrylak. Exciton lifetime in InAsGaAs quantum dot molecules. *Physical Review B*, 72(3), jul 2005.

[63] Tobias Huber, Laurin Ostermann, Maximilian Prilmüller, Glenn S. Solomon, Helmut Ritsch, Gregor Weihs, and Ana Predojević. Coherence and degree of time-bin entanglement from quantum dots. *Phys. Rev. B*, 93:201301, May 2016.

[64] Luca Salasnich. *Quantum Physics of Light and Matter.* Springer International Publishing, 2017.

[65] Roy J. Glauber. Coherent and incoherent states of the radiation field. *Physical Review*, 131(6):2766–2788, sep 1963.

# List of Figures

1.1 Left: schematics of the capping process of quantum dots. Right: image of self-assembled quantum dots . . . 2
1.2 Image of site-controlled quantum dots . . . 3
1.3 Example of the configuration used during the thesis project . . . 4
1.4 Density of states as function of the energy for different system dimensions 4
1.5 Schematics of the main bound states in a quantum dot . . . 7
1.6 Schematics of the energy splitting of the exciton . . . 8
1.7 Above band excitation schemes . . . 9
1.8 Emission rate as function of the mean number of excitations . . . 11
1.9 In-band excitation schemes . . . 12
1.10 Rabi oscillations for different values of dephasing . . . 13
1.11 Two-photon resonant excitation scheme . . . 14
1.12 Photon time distribution for different types of sources . . . 15
1.13 Second order correlation function $g^{(2)}(\tau)$ for different kind of sources . . . 18
1.14 Experimental setup used for a Hanbury-Brown-Twiss measurement . . . 19
1.15 $g^{(2)}(\tau)$ for different kind of excitation. Left: continuous excitation. Right: pulsed excitation . . . 19
1.16 Experimental setup used for Hong-Ou-Mandel interference . . . 20
1.17 Ways two photons can interact with a beam splitter . . . 21
1.18 Result of the HOM interference . . . 22

2.1 Fermi distribution at different values of $E_F/k_BT$ . . . 23
2.2 Density of electrons in conduction band at different temperatures . . . 24
2.3 Optical line built for the imaging and the excitation of the quantum dot . 26
2.4 Image of the sample . . . 26
2.5 Princeton instruments spectrometer . . . 27
2.6 Screenshot from the Princeton spectrometer software . . . 27
2.7 Scheme of a blazed diffraction grating . . . 28
2.8 Self-made spectrometer . . . 29
2.9 Propagation of a gaussian beam along an axis z . . . 31
2.10 Schematics of razor blade technique and result of the measurement . . . 32
2.11 Design of the optical line and the pulse stretcher . . . 34
2.12 3D view of the project realized with Zemax Optic Studio . . . 35
2.13 Slit part of the project realized with Zemax, and the final *Spot diagram* . 36
2.14 Spectrum of the Ti:Sapphire laser . . . 37

2.15 Spectrum of the laser after the pulse stretcher . . . . . . . . . . . . . . . . . 38
2.16 FWHM of the spectrum at different positions of the slit . . . . . . . . . . . 38
2.17 Michaelson interferometer . . . . . . . . . . . . . . . . . . . . . . . . . . . . 39

3.1 Spectra of the quantum dot, at different excitation powers . . . . . . . . . 46
3.2 Power dependence of intensity of the exciton and biexciton lines . . . . . 47
3.3 Spectrum of the quantum dot before and after removing the background . 48
3.4 Measurement of the second order correlation function for the exciton photons 49

4.1 Example of Rabi oscillations . . . . . . . . . . . . . . . . . . . . . . . . . . . 52